# The iron oxidation state of Ryugu samples

Mathieu Roskosz, Pierre Beck, Jean-christophe Viennet, Tomoki Nakamura, Barbara Lavina, Michael Y Hu, Jiyong Zhao, Esen E Alp, Yoshio Takahashi, Tomoyo Morita, et al.

# The iron oxidation state of Ryugu samples

Mathieu Roskosz[1], Pierre Beck[2], Jean-Christophe Viennet[1], Tomoki Nakamura[3], Barbara Lavina[4,5], Michael Y. Hu[5], Jiyong Zhao[5], Esen E. Alp[5], Yoshio Takahashi[6], Tomoyo Morita[3], Kana Amano[3], H. Yurimoto[7], T. Noguchi[8], R. Okazaki[9], H. Yabuta[10], H. Naraoka[9], K. Sakamoto[11], S. Tachibana[6], T. Yada[11], M. Nishimura[11], A. Nakato[11], A. Miyazaki[11], K. Yogata[11], M. Abe[11], T. Okada[11], T. Usui[11], M. Yoshikawa[11], T. Saiki[11], S. Tanaka[11], F. Terui[12], S. Nakazawa[11], S.-I. Watanabe[13], Y. Tsuda[11]

**[1]Institut de Minéralogie, Physique des Matériaux et Cosmochimie, Muséum National d'Histoire Naturelle, Sorbonne Université, CNRS UMR 7590, Paris, France.**

**[2]Institut de Planétologie et d'Astrophysique de Grenoble, Université Grenoble Alpes, Grenoble, France.**

**[3] Tohoku University, Sendai 980-8578, Japan.**

**[4]Center for Advanced Radiation Sources, The University of Chicago, Chicago, USA**

**[5]Advanced Photon Source, Argonne National Laboratory, Argonne, USA**

**[6] The University of Tokyo, Tokyo 113-0033, Japan**

**[7] Hokkaido University, Sapporo 060-0810, Japan**

**[8] Kyoto University, Kyoto 606-8502, Japan**

**[9] Kyushu University, Fukuoka 819-0395, Japan**

**[10] Hiroshima University, Higashi-Hiroshima 739-8526, Japan**

**[11] Institute of Space and Astronautical Science (ISAS), Japan Aerospace Exploration Agency (JAXA), Sagamihara 252-5210, Japan**

**[12] Kanagawa Institute of Technology, Atsugi 243-0292, Japan**

**[13] Nagoya University, Nagoya 464-8601, Japan**

**Corresponding author: E-mail address: mathieu.roskosz@mnhn.fr.**

# Abstract

The Hayabusa2 mission sampled Ryugu, an asteroid that did not suffer extensive thermal metamorphism, and returned rocks to Earth with no significant air exposure. It therefore offers a unique opportunity to study the redox state of carbonaceous Cb-type asteroids and evaluate the overall redox state of the most primitive rocks of the solar system.

An analytical framework was developed to investigate the iron mineralogy and valence state in extraterrestrial material at the micron scale by combining X-ray diffraction, Conventional Mössbauer (MS) and Nuclear Forward Scattering (NFS) spectroscopies. An array of standard minerals was analyzed and cross-calibrated between MS and NFS. Then, MS and NFS spectra on three Ryugu grains were collected at the bulk and the micron scales.

In Ryugu samples, iron is essentially accommodated in magnetite, clay-minerals (serpentine-smectite) and sulfides. Only a single set of Mössbauer parameters was necessary to account for the entire variability observed in MS and NFS spectra, at all spatial scales investigated. These parameters therefore make up a fully consistent iron mineralogical model for the Ryugu samples. As far as MS and NFS spectroscopies are concerned, Ryugu grains are overall similar to each other and share most of their mineralogical features with CI-type chondrites. In detail however, no ferrihydrite is found in Ryugu particles even at the very sensitive scale of Mössbauer spectroscopy. The typical $Fe^{3+}/Fe_{tot}$ of clay minerals is much lower than typical redox ratios measured in CI chondrites ($Fe^{3+}/Fe_{tot}$=85-90%). Furthermore, magnetite from Ryugu is stoichiometric with no significant maghemite component, whereas up to 12% of maghemite was previously identified in the Orgueil's so called magnetite. These differences suggest that most CI meteorites suffered terrestrial alteration and that the pre-terrestrial composition of these carbon-rich samples was less oxidized than previously measured. However, it is not clear yet whether or not the parent bodies of CI chondrites were as reduced as Ryugu.

Finally, the high spatial resolution of NFS allows to disentangle the redox state and the crystal-chemistry of iron accommodated in serpentine and smectite. The most likely polytype of serpentine is lizardite, containing less than 35% of $Fe^{3+}$, a fraction of which being tetrahedrally coordinated. Smectite is more oxidized ($Fe^{3+}/Fe_{tot}$>65%) and mainly contain octahedral ferric iron. This finding implies that these clays formed from highly alkaline fluids and the spatial-variability highlighted here may suggest a temporal evolution or a spatial variability of the nature of this fluid.

# 1. Introduction

The valence state of iron is a historical tool in the construction of present day classification of chondritic meteorites, and the abundance of "metallic" iron ($Fe^0$) with regard to more oxidized iron species ($Fe^{2+}$ and $Fe^{3+}$) is still used today in the taxonomy of chondritic meteorites (Krot et al., 2007). However, down to the micron scale, chondrites are assemblages of heterogeneous components that are not in thermodynamical equilibrium. The initial iron budget was set by the nature and relative abundance of the accreted constituents and was subsequently modified by geological processes on the meteorites parent bodies. During and after their accretion, thermal metamorphism and aqueous alteration triggered partial textural and chemical re-equilibrations together with mineralogical transformations. For instance, in most recovered chondrites, silicates are partially recrystallized and metallic grains are often transformed into oxides and hydroxides (Brearley et al., 2006, Garenne et al., 2019; Nakamura et al., 2005). As a consequence, the initial states of the different components are not directly accessible. However, it is generally assumed that the various chondrite groups sampled different types of materials and record different redox conditions in the protosolar nebula, as a result of different distances to the sun, formation time, carbon-content or dust to gas ratio.

Meteorites offer a natural sampling of asteroidal bodies and our understanding of the composition of asteroids strongly relies on the comparison of their telescopic spectra to those acquired from meteorites on Earth. The most widely used spectral range is between 0.5 and 2.5 µm, that is central to the most recent asteroid taxonomies (DeMeo et al., 2009, Mahlke et al., 2022). In that spectral range all key absorptions used to link meteorites to their asteroidal counterparts are related to the Fe-mineralogy. In particular, the presence of iron in anhydrous silicates (olivine and pyroxene) induces crystal field absorptions around 1 and 2 µm that defines members of the S-class (Gaffey et al., 2002), the visible to infrared spectral slope of some X-type object is likely related to the optical constants of Fe-metal or Fe-sulfides (Vernazza and Beck, 2017), while the absorptions observed around 0.7 and 0.9 µm are diagnostic of $Fe^{2+}$and $Fe^{3+}$ in phyllosilicates (Vilas et al., 1994). This understanding of asteroid composition thus relies on the meteorite sample available, but this sampling is biased by dynamical effects (resonances) and the presence of the terrestrial atmosphere that may filter meteoroids as a function of their strength. The comparison may also be blurred by the action of space-weathering processes that modify the surface mineralogy of airless bodies, and by the alteration of meteorites on Earth when exposed to terrestrial atmosphere. In this context, the Hayabusa2

mission sampled Ryugu, an asteroid that did not suffer extensive thermal metamorphism, and returned rocks to Earth with no significant air exposure (Tachibana et al., 2022; Okazaki et al., 2022). Furthermore, contrary to the Stardust mission that returned cometary grains, Ryugu samples were not heavily thermally-modified during the collection (e.g. Roskosz et al., 2008; Leroux et al., 2009; Noguchi et al., 2022). Also, a substantial fraction of the collected Ryugu samples are much larger than particles collected from Itokawa and are therefore not dominated by space-weathered materials (Noguchi et al., 2011). It therefore offers a unique opportunity to study the redox state of carbonaceous Cb-type asteroids (Ito et al., 2022; T. Nakamura et al., 2022; E. Nakamura et al., 2022; Yokoyama et al., 2022) and evaluate the overall redox state of the most oxidized primitive rocks of the solar system.

Mössbauer spectroscopy (MS) has been widely used in Earth science and material science to probe the crystal-chemistry of Fe bearing samples, but has been limited to rather large samples using conventional setups (>0.5 mm typical). With the advance of synchrotron radiation, its time domain analog, Nuclear Forward Scattering (NFS), has emerged and been widely applied (Shvyd'ko, 1999). This method involves first nuclear resonant transitions of Mössbauer nuclei excited by synchrotron radiation, and then the recording of the time spectrum following the decay of excited nuclei. The collected coherent nuclear resonant scattering signal provides measurements of hyperfine interactions of the nuclei in the solid, which lead to quantitative and absolute information about the magnetic, valence and spin states of the system, and local atomic symmetry for all the possible valence state of iron. It is sensitive to the chemical environment of Mössbauer isotopes ($^{57}$Fe in our case) and has been an effective tool for studying the magnetic and chemical structure of materials, inorganic and organic, crystalline and amorphous alike. This synchrotron radiation based method allows imaging samples at the micrometer spatial resolution. However, despite continued advance of this method over past decades, the use of this spectroscopy in the field of cosmochemistry is very limited (e.g. Blukis et al., 2017).

Here, we shortly introduce this spectroscopy. Key minerals used for the analysis of extraterrestrial samples are analyzed by conventional Mössbauer Spectroscopy and Nuclear Forward Scattering to build a database available for the entire community. The consistency of the results collected by both methods is assessed. The fitting procedure to be applied to NFS spectra collected on natural samples is established. Additional analytical techniques such as the use of an external magnetic field to access subtle features in complex NFS spectra of meteorites are introduced. Then, MS and NFS spectra collected on 3 different Ryugu grains (2 from the first touchdown site and 1 from the second touchdown site) are presented and quantitatively

discussed. Limited MS and NFS results of Ryugu samples were shown in a first report (T. Nakamura et al., 2022). In the present study, more comprehensive results including new analysis and a new sample are presented. Bulk oxidation states of major Fe-bearing minerals are derived for each samples and spatial variations are highlighted. Our results show similarities but also some significant differences as compared to the most common CI materials (Orgueil and Alais meteorites), to which the Ryugu samples are most similar (e.g., Yokoyama et al., 2022; T. Nakamura et al., 2022). The likely nature and redox states of the main clay minerals (serpentine and smectite) is discussed in the light of Mössbauer parameters and the highly alkaline nature of the fluids from which these clays formed is assessed.

# 2. An overview of Nuclear Forward Scattering

Nuclear forward Scattering (NFS) is a relatively new spectroscopic technique that allows one to probe the valence, structural and magnetic states of certain elements in solids. An in-depth description of the physics of this spectroscopy can be found in Sturhahn (2004) and a more geophysically-oriented introduction is in Sturhahn and Jackson (2007). Its use in Earth sciences has mostly focused on high-pressure mineral physics applications to determine the behavior of iron in mantle and core forming minerals. The NFS method shares most aspects with the conventional Mössbauer Spectroscopy (MS) and relies on the fact that $^{57}$Fe possesses a low-lying nuclear excited state at 14.4125 keV that can be populated by X-ray photons of the appropriate energy without participation of lattice vibrations (so-called recoilless absorption). In MS, these photons are produced by a source that contains radioactive $^{57}$Co, which first decays into excited $^{57}$Fe* and then to the ground state, thus emitting a photon of the exact energy to excite $^{57}$Fe in the target material. This emission of photons is random in time but the energy bandwidth is extremely narrow (4.66 neV). In NFS, the exciting radiation comes from a bright X-ray beam produced by a synchrotron source. The primary beam is intense, pulsed and short (pulse length <100 ps), and periodical (e.g. every 153 ns for standard operation mode at the Advanced Photon Source – APS – Argonne National Laboratory, USA). However, the energy spectrum is very broad, covering many keVs. After it passes through two monochromators, the energy spread is reduced to only about 1 meV which is still large as compared to the natural line width. While MS is energy-resolved whereas NFS is time-resolved, their energy and time characteristics (Fig. 1a) illustrate the fact that these two techniques are roughly reciprocal, with a crucial difference of loss of phase information in MS. In both cases, relevant hyperfine parameters for minerals can be determined. The isomer shift (IS) originates from the electron density difference at the nucleus and is indirectly influenced, via shielding effects, by the d-electrons in the valence shell, thus allowing to infer the oxidation state. The nuclear quadrupole splitting (QS or $\Delta$) results from a non-vanishing electric field gradient at the Mössbauer nucleus occupying a state with an angular momentum quantum number $I > 1/2$. The QS yields information on the local coordination environment and, complementary to the isomer shift, oxidation and spin states of the atom can be deduced. Finally, in the presence of an internal or external magnetic field, spin degeneracies of both ground and excited nuclear levels are lifted resulting in magnetic splitting (HT), which gives a measure of the magnetic field.

In order to collect NFS spectra, some technical achievements had to be reached. Indeed, during the X-ray illumination of the $^{57}$Fe nuclei in the target, most of the incident beam is scattered by electronic shells without interaction with the Fe nuclei. The signal from these photons is almost instantaneous (on the order of ps and fs). Nuclear resonant cross section is many orders of magnitude larger than electronic scattering but in a much narrower energy bandwidth. Nonetheless, advantage of this resonant enhancement is taken at modern synchrotron radiation facilities producing adequate spectral flux. The relatively much longer lifetime of excited Mössbauer level, 141 ns for $^{57}$Fe, permits time filtering using timing detectors and electronics. Because the primary beam is pulsed (e.g. 153 ns between pulses, each of 70 ps duration in standard APS operation mode), it is possible to apply time discrimination on the scattered signal in order to remove the electron contributions and only retain the time-delayed nuclear resonant scattering signal (Fig. 1b) resulting in extremely low background spectra. The first successful NFS experiment was achieved in 1991 (Hastings, et al., 1991). Since then, brighter undulator sources, improvements in X-ray optics, timing detectors and electronics, together with data analysis software have made this spectroscopy method practical and is now considered a fully matured technique. This is documented by its applications in a broad range of basic and applied research areas.

# 3. Sample selection and analytical procedures

## *3.1. Sample selection*

An array of key minerals was analyzed during three beamline sessions together with three meteoritic samples, namely Orgueil (CI), Alais (CI) and Tagish lake (Ungrouped CC). Minerals relevant for cosmochemical studies were loaned by different collaborators and institutions (Namely M. Zolensky, NASA, USA; C. Engrand, CSNSM, France; IPAG, France; MNHN, France). Samples were large single crystals and mm-size chunks of meteorites (Table 1). Because the MS and NFS spectra of large crystals would results in artificially broad lines and because NFS spectra are polarized in nature, small piece of each of them were gently crushed in an agate mortar and the resulting coarse powders were loaded in a pierced (1-2 mm in diameter) lead foil used as a sample holder for both NFS and MS analysis. Standards were analyzed just after this conventional preparation step, which is not known to lead to significant oxidation of the samples.

Turning to Hayabusa2 samples, four beamline sessions were dedicated to the study of three different grains. Grains C0061 (~0.9*0.5 mm; 1.65 mg), A0026 (~3*2 mm; 3.9 mg) and A0117 (~3*2 mm; 4.2 mg) were provided by the Extraterrestrial Sample Curation Center (ESCuC), ISAS, JAXA, Japan. So-called grain C comes from chamber C of the Hayabusa2 spacecraft and was collected at the second collection site on the asteroid. They may represent sub-surface material exposed by the impactor. Grains A were recovered from chamber A and were collected during the first touchdown. Grains C0061 and A0026 were transferred under nitrogen from ESCuC to Tohoku University. Half of the grain C0061 (that was originally mm-sized) and grain A0026 were sealed in an airtight plastic container in a glove box with a low dew point (<−60 °C) and low oxygen pressure (<10 ppm). Grain A0117, also transferred under nitrogen, arrived at the Muséum National d'Histoire Naturelle from ESCuC in a stainless-steel container (so-called FFTC). A subgrain of several hundreds of micrometers was detached from the main mm-size mass A0117. To recover the sub-grain of A0117 studied here (named hereafter A0117B) and to avoid any exposure to terrestrial atmosphere, the FFTC was transferred in a dry glove box (<0.5 ppm $H_2O$ and <0.5 ppm $O_2$) and under 0.9 mbar of Ar atmosphere (IMPMC, France). Then, the grain was sealed, in the glovebox, in a plastic bag using a vacuum seal bag. All the samples analyzed here where thus characterized before any exposure to terrestrial air through the plastic bags. Since the mineralogy of Ryugu is essentially

fine grained (e.g. T. Nakamura et al., 2022), there was no need to crush the samples to avoid line broadening and/or polarization artefacts in the collected spectra.

*3.2. Conventional MS and Synchrotron NFS data collection and treatment*

Conventional energy-domain $^{57}$Fe Mössbauer spectroscopic experiments were conducted at the Advanced Photon Source, Argonne National Laboratory using a $^{57}$Co/Pd source of approximately 5 mCi strength. Spectra were collected at 1 bar atmosphere and 298 K on powders or small chunks. The data was obtained using constant acceleration mode with a Vortex silicon drift detector with an energy resolution of 150 eV at 14.4 keV in order to reduce background. The data was analyzed using WinNormos (Wissel Co.) program. As described below, chondritic materials exhibit complex polyphasic MS spectra. For his reason, we established a systematic fitting procedure used for all the samples. First, site ratios of all phases were refined, then we proceeded adjusting magnetite hyperfine parameters, as outermost magnetite lines do not overlap with any other phases lines. Area ratios between A and B sites in magnetite were allowed to change arbitrary. Pyrrhotite sites were then slightly adjusted from the starting model, and finally silicate parameters were released. Ryugu particles (with the exception of C0061) were small and consequently the obtained MS spectra had low signal/noise ratios. For this reason, instead of carrying out fitting procedures without any *a priori* trial parameters, we used the mineralogical model determined on the large C0061 particle to adjust the best fit to the two other spectra. The relative areas of each line were the only adjustable parameters. Additional tests, including free variations of other parameters were carried out in order to confirm the robustness of the model obtained following this methodology.

The NFS measurements were conducted at the Beamline 3-ID-B of the Advanced Photon Source (APS), Argonne National Laboratory. The storage ring was operating in top-up mode with 24 bunches separated by 153 ns. A high-resolution monochromator was tuned to the 14.4125 keV nuclear transition energy of $^{57}$Fe with a FWHM of 1 meV (Toellner, 2000). The beam was focused to an area of 20 by 20 μm$^2$ using a Kirkpatrick-Baez mirror system (Zhang et al., 2015). The time spectra were measured with an avalanche photodiode detector, positioned ~0.5 m downstream from the sample in the forward direction. A time window of roughly 21 to 128 ns after excitation was used to observe nuclear resonant scattering. A stainless steel (SS) foil was placed in the downstream direction as a reference absorber for isomer shift measurements.

All the fits to the time spectra and time-to-energy spectra conversion were performed

using the CONUSS program (Sturhahn, 2000). Fits to the data were produced by using the mineralogical model established from conventional Mössbauer spectra. Parameters were sequentially optimized, phase after phase, starting from magnetite, then focusing to silicates and pyrrhotite, iteratively. Some of the parameters such as the relative proportions of A and B sites in magnetite were released and optimized late in the procedure, only after reasonable convergence was already achieved. This was done because the number of free parameters to optimize from NFS spectra greatly exceeds the amount of information available in a given spectrum. For this reason, different local optimization minima exist in the optimization landscape, most of them can be rejected, providing mineralogically meaningless outputs such as, for instance, magnetite with no B sites or pyrrhotites exhibiting only one sextet. For this reason, the self-consistency between all MS and NFS fitting parameters was a major criterion used to evaluate the quality of the fits. Nonetheless, all the parameters were ultimately adjusted.

### *3.3. X-ray diffraction data collection and treatment*

The experimental station 3-ID-B of the Advanced Photon Source, Argonne national Laboratory, is equipped with an Eiger 2 X 500K area detector that was used to collect diffraction data in combination with NFS data. Hence, diffraction data were collected with the same beam energy and size described for NFS measurements. The detector was calibrated against the powder diffraction patterns of $CeO_2$ or $LaB_6$ standards. Detector calibration and data reduction were performed using Dioptas (Presher and Prakapenka, 2015).

# 4. Results

## *4.1 Assessment of the self-consistency between MS and NFS on mineral standards*

In order to validate our analytical approach, a suite of reference minerals (Table 1) was analyzed using both MS and NFS with the idea to evaluate the self-consistency between the parameters determined from the fit to the conventional NFS data. This suite of samples was defined in order to test different environment and valence state of iron atoms ($Fe^{2+}$, $Fe^{3+}$, magnetic phase) and to represent the dominant mineral phases found in Ryugu samples. Therefore, they include two serpentines (clino-chrysotile and Modum serpentine, Norway), an Fe-bearing smectite, anhydrous silicates (Mg- and Fe- rich olivine, augite) and last, a magnetite sample. They were selected because they are homogeneous and well crystallized at the mm-scale and do not exhibit inclusions or intermingled secondary phases. However, their redox state was not previously analyzed. This is an additional reason for paying special attention to the fits to the MS data collected on these samples. The spectra obtained are displayed in Figure 2 and Figure 3 and the Mössbauer parameters retrieved from this analysis are given in Table 2.

As explained above, NFS data are time spectra due to coherent interference of decays of different hyperfine energy levels, resulting in certain beating patterns depending on the specifics of the environment of the iron atoms. Generally, $Fe^{3+}$ ions in non-magnetic sites have a low quadrupole splitting, resulting in a single minimum in the time window investigated. This behavior can be observed for $Fe^{3+}$-smectite and the Modum serpentine (Fig. 3). In the case of $Fe^{2+}$ ions in non-magnetic sites, the quadrupole splitting value is higher, resulting in two to three beats in the time window investigated. This can be seen for the two olivines, the augite as well as the clino-chrysotile, for which $Fe^{2+}$ is the most abundant valence state of iron atoms as attested by MS (Fig. 2, Table 2). In the case of magnetite, which presents two sites with different hyperfine splitting values, the NFS spectrum is much more complex (Fig. 3).

For all samples, high-quality and robust fits could be obtained for both types of measurements. In detail, divalent cations can occupy two non-equivalent sites in the olivine crystal structure (e.g. Dyar et al., 2009). In iron-rich olivine, both sites are occupied by $Fe^{2+}$ atoms. Here consequently, in the case of $Fe^{2+}$-rich olivine, our spectra were modelled with two sites as it was previously proposed by Bancroft et al. (1967). The spectral modelling showed good consistency in the relative abundance of the two sites (within 2 % between the two techniques) as well as for the retrieved values for the QS and IS (Fig. 2, Table 2). In the case of the Fe-poor San Carlos olivine, only one site could be resolved with a QS higher than the mean

of the QS for the two sites of the $Fe^{2+}$-rich olivine. The decrease of QS with increasing iron content was also reported previously (Bancroft et al., 1967).

The MS data obtained on the augite crystal were best described with two sites for iron atoms, the most populated one has a high QS and is attributed to $Fe^{2+}$. The second one exhibits a lower QS typically attributed to $Fe^{3+}$. Contrary to olivine, accommodation of $Fe^{3+}$ in clino-pyroxene (augite) is significant (Rudra and Hirschmann, 2022). Based on our fits to the data, the fraction of $Fe^{3+}$ derived from the two techniques (MS and NFS) are not identical but reasonably close (5.8 % vs 9.8 %). The absolute values for QS and IS obtained from the models are also close (Table 2). Note finally that we could not distinguish the two possible sites for $Fe^{2+}$ in our analysis.

The three studied hydroxylated minerals showed distinct spectral features. In the case of the $Fe^{3+}$-smectite and the Modum serpentine, the MS data could be accounted for with one ($Fe^{3+}$-smectite) or two sites (Modum spectra) with low QS, hence typically attributed to $Fe^{3+}$. For the smectite, while only a single site was needed for the MS spectrum, three sites with low QS value had to be used to obtain a satisfying fit to the NFS spectrum (Table 2). Still, both types of measurements reveal that the iron budget is strongly dominated by $Fe^{3+}$ in this sample and that no significant amount of $Fe^{2+}$ was detected. In the case of the Modum serpentine, the Mössbauer parameters derived from MS and NFS, and the fraction of each site, are in fair agreement (Table 2). The clino-chrysotile sample was best modelled with two sites in both Mössbauer techniques, a dominant one attributed to $Fe^{2+}$, and a second one with a lower QS and assigned to $Fe^{3+}$. Again, the Mössbauer parameters used to adjust the best fit to the data are in good agreement between the two techniques (Table 2).

Last, Mössbauer spectra were obtained on a magnetite sample with the two analytical approaches. Unlike phases above-mentioned, magnetite is a magnetic phase at room temperature leading to complex hyperfine splitting. Typically, MS spectra exhibit several peaks formed by series of sextets. The spectra were successfully modelled and the fraction of sites and Mössbauer parameters (IS, QS, HT) derived from both methods are consistent (Table 2). Note that the magnetite studied here deviates from its normal stoichiometry and is over oxidized. In other words, the studied mineral contains a significant maghemite component, which is common in terrestrial natural samples. More importantly, such non-stoichiometric magnetite is reminiscent of the magnetite crystals analyzed in the Orgueil CI meteorite (Madsen et al., 1986, 1989, Gunnlaugsson et al., 1994) and therefore makes a relevant standard mineral in cosmochemistry.

*4.2 On the use of an external field in samples containing magnetic phases*

Ryugu samples are polymineralic, the presence of multiple partially-overlapping lines, hampers the uniqueness of spectra interpretation. Since the samples contain both magnetic and non-magnetic phases, we applied a technique to *simplify* the Mössbauer spectra and facilitate the fitting process. In this technique, samples are placed in a strong magnetic field while collecting NFS spectra. At specific orientations of the magnetic field with regard to the polarization of the synchrotron radiation, selected energy level transition can become forbidden, thus simplifying the collected spectrum. In our case, we applied a magnetic field of 0.78 T, perpendicular to the polarization direction of the synchrotron beam, which leads to extinction of $\Delta m=+1$ and $\Delta m=-1$ transitions. This approach was tested on a powdered sample from the Tagish Lake ungrouped carbonaceous chondrite, known to be rich in phyllosilicate and magnetite (Herd et al., 2011). The NFS spectrum collected without magnetic field reveals a complex pattern from which a reasonably robust fit could be obtained. Once a magnetic field is applied, the NFS spectrum simplifies, and a fit of higher quality and robustness was obtained (Fig. 4). Mössbauer parameters derived from NFS spectra were then used to calculate the corresponding MS spectra (Fig. 4). This figure reveals that typical sextets describing magnetite are turned into doublets when the magnetic field is applied. This simplification of the spectrum, reduces peak overlapping especially in the central part of the MS spectrum, where ferrous and ferric non-magnetic contributions are typically observed. This facilitates the spectrum interpretation and, more importantly, offers an improved description of these non-magnetic doublets (i.e. a better evaluation of their IS, QS and area fractions). For this reason, when available parameters and models derived from this technique should supersede those obtained from more classical data acquisition protocols. Nevertheless, since, within uncertainty, the same information should be derived from spectra collected on the same sample by different techniques, efforts were payed to propose, as far as possible, self-consistent series of fits for a given sample.

*4.3. X-ray diffraction analysis of Ryugu particles*

The mineralogy of the grains was first determined by XRD measurements prior to any exposure to air. Samples were analyzed in their *sealed plastic bags,* prepared in the curation facility in a dry $N_2$ atmosphere. This explains the presence of the diffraction peaks labelled "plastic bags" (Fig. 5). Note that this attribution is based on the separate XRD analysis of the

plastic bags. As two different kinds of polymers were used for grains A0026, C0061 and A0117B peak positions are different in the corresponding diffraction patterns. Based on XRD patterns, the major phases present in grains A0026, C0061, A0117B are clay minerals, magnetite, pyrrhotite, pentlandite and dolomite (Fig. 5). This mineralogy is typical of the Ryugu grains (T. Nakamura et al., 2022; Viennet et al., 2023).

Focusing here on the clay mineralogy, the XRD reflection at 4.59 Å is related to the typical 02.11 reflections of Mg-rich trioctahedral clay minerals. The clay mineralogy is made of a mixture of serpentine and smectite. Indeed, the peaks at ~7.3 and 3.6 Å correspond to the 001 and 002 reflections of serpentine while the peaks at 12.44 and 3.13 Å correspond to the 001 and 004 reflections of a smectite-rich minerals (Viennet et al., 2023).

In detail, differences exist between the grains. While the intense 001 reflections are easily distinguishable for the grain C0061, this reflection is weak for the grain A0026 and A0117B. This observation implies either a larger content and/or a higher coherent scattering domain size of the smectite-rich minerals (i.e. better crystallized) for the grain C0061. Note also that, the focused measurement made on grain A0117B (A0117-polarized) does not present contribution of smectitic clay minerals. This peculiar location will be used later to evaluate the redox states of serpentine and smectite individually. Furthermore, a significant variability is found in the serpentine minerals between the grains. Compared to grain C0061, the 001 reflections of serpentine for the other grains are larger and slightly shifted to lower angles (Fig. 5). This effect is typical of apparent irrationality (Drits and Tchoubar 2012), which shows a lower degree of crystallinity of those serpentine minerals in all the A grains as compared to C0061. In conclusion, grain C0061 presents a higher crystallinity of both smectite and serpentine, and a higher content of smectite-rich clay minerals as compared to the A0026 and A0117B grains. Conversely, the focused point for the polarized NFS measurements of grain A0117B does not exhibit the presence of smectite.

### *4.4. Bulk analysis of Ryugu particles by conventional Mössbauer spectroscopy*

Conventional energy-domain $^{57}$Fe Mössbauer spectroscopic experiments were conducted at 1 bar atmosphere and 298 K. Samples C0061, A0026 and A0117B were analyzed. The acquisition time was typically of a couple of weeks in order to get sufficiently good signal/noise ratios. Even in these conditions, precise and accurate mineralogical information could only be derived for sample C0061. The other spectra are of acceptable quality but given the complexity of the iron mineralogy in Ryugu, unique fits to the data could only be produced

419 on C0061 (Fig.6).

420 A starting model for the interpretation of the C0061 spectrum was based on the bulk
421 mineralogy derived by XRD (Fig. 5 and T. Nakamura et al., 2022; Viennet et al., 2023).
422 Magnetite, pyrrhotite and silicates containing both ferric and ferrous iron were considered as
423 iron-bearing phases. Magnetite was first modelled using 2 sextets with the hyperfine parameters
424 obtained from stoichiometric magnetite (Table 3). Pyrrhotite was found to be a 4C polytype in
425 Ryugu (T. Nakamura et al., 2022) so we used a simplified three sextets model for 4C polytype
426 after Jeandey et al. (1991). Finally, Fe-bearing silicates were initially modeled with two
427 doublets as observed for Orgueil (Madsen et al., 1986 and see below for a reappraisal). The
428 model, consisting of 7 sites and 24 parameters, was refined cautiously by optimizing parameters
429 sequentially following the procedure described in the previous section. An excellent fit was
430 eventually achieved (Fig. 6, Table 3).

431 The two other grains were smaller than C0061 and consequently the obtained MS
432 spectra had lower signal/noise ratios. For this reason, instead of carrying out fitting procedures
433 without any *a priori* trial parameters, we used the mineralogical model determined on C0061
434 to adjust the best fit to the two other spectra. We found that the mineralogical model defined
435 for C0061 is robust enough to provide a self-consistent description of the iron mineralogy and
436 redox-state in Ryugu particles at the grain scale. No other mineralogical model could provide
437 better fits. This model (Table 3) suggests that the iron mineralogy is indeed dominated by
438 stoichiometric magnetite, pyrrhotite 4C and mixed-valence Fe-bearing silicates. No additional
439 lines were needed to account for any spectral features. No significant magnetite non-
440 stoichiometry was found to improve the quality of the fits. In other words, contrary to Orgueil
441 for which the ratio of A and B sites in magnetite differs from the 1/3 – 2/3 nominal abundances
442 (Madsen et al., 1986, and see discussion below), Ryugu's magnetite does not seem to be over-
443 oxidized. The parameters describing the three lines of pyrrhotite are also broadly consistent
444 with hyperfine parameters obtained on 4C-polytypes (Jeandey et al., 1991). Finally, good fits
445 to the central peaks could be produced assuming only two symmetrical doublets for silicates,
446 one with hyperfine parameters typical of $Fe^{2+}$ in six-fold coordination and a second line more
447 typical of $Fe^{3+}$ in four-fold coordination (e.g. Dyar and Sklute, 2019). These two lines are
448 slightly broader than theoretical ones but there is not enough information in the spectrum to add
449 more doublets to the fit and thus to resolve the iron mineralogy of each coexisting silicate and
450 to take into account possible textural factors such as crystal size or anisotropy. For this reason,
451 it is considered here that the conventional Mössbauer spectra do not help to point to the redox
452 state of each Fe-bearing silicate reported by XRD analysis, namely serpentine, smectite (and

possibly traces of olivine).

### *4.5 Bulk analysis of Ryugu particles by NFS: Toward a unified iron mineralogical model for asteroid Ryugu*

Samples C0061 and A0026 were probed by NFS operated with an unfocused beam, providing spectra representing the whole grains mineralogy. These measurements were carried out in the polarized and unpolarized configurations introduced previously (Fig.7). Fits to the data were produced following the fitting procedure described previously. All the spectra could be successfully modelled using the mineralogical model established for C0061 with small variations in the parameters, further strengthening the robustness of the model (Table 3).

The Mössbauer parameters (quadrupole splitting, isomer shift, and magnetic hyperfine splitting) derived from our analysis of both MS and NFS measurements, using a mineralogical model with 3 phases (magnetites, pyrrhotites, and clay minerals) corresponding to 7 distinct environments of iron atoms are displayed in Figure 8. Overall, the Mössbauer parameters obtained through the recursive processing of NFS and MS spectra are fairly similar, and our mineralogical model for iron mineralogy is consistent for the whole dataset obtained. In other words, the 7 endmembers describe our dataset obtained on Ryugu samples, and the variability observed can be explained by varying the proportions of each endmembers (i.e. variation of proportions of the three phases, and limited variation of the site distribution in each phase).

From this analysis, proportions of iron in each of the three phases was derived (Figure 9). The two major carriers of Fe are magnetite and clay-minerals, while the fraction of iron accommodated within pyrrhotite is present in a lower amount (16-23 at.% which can be seen as roughly constant among our samples given our estimated analytical error). The fraction of iron in clay-minerals and magnetite is more variable, (24-44 at.% for clays and 38-59 at.% for magnetite). The proportion of magnetite obtained for grain C0061 using MS data is slightly lower than those obtained using NFS measurements (Fig. 9). This could be coincidental or due to the fact that MS measurements were carried on an even larger area (the whole grain) than NFS (even unfocused). The presence of a few large grain of magnetite in the area analyzed with NFS (nugget effect) could possibly explain this difference. In the case of grain A0026, the two analytical approaches lead to consistent results within analytical error.

### *4.6 Local variability of the mineralogy revealed by focused NFS*

The use of a bright synchrotron source instead of a conventional gamma source offers the opportunity to obtain high quality spectra from small samples and to investigate lateral variations of the iron mineralogy and/or of the redox state of minerals at the micron scale. Focused NFS spectra were collected on all grains (Fig. 7 and Fig. 10). The same mineralogical model can account for the limited yet significant spectral variability. In other words, a variation of the relative proportions of the Fe-bearing phases can explain most of the variability highlighted here. We note however that the relative proportions of the three lines of pyrrhotite varies from one region of interest (ROI) to the other and might indicate that different types of pyrrhotite crystals or textures might coexist. Further detailed study of pyrrhotite would be necessary to confirm this hypothesis. The same remark holds true for magnetite. In this case, at least two microstructures were observed by microscopy (T. Nakamura et al., 2022; Dobrică et al., 2023) and taken as an indication that these minerals formed in different petrological contexts (Dobrică et al., 2023; Aléon et al., 2023). Turning to silicates, one spectrum is of particular interest, namely the A0117B NFS polarized and focused spectrum (Fig. 7). It exhibits a significantly lower intensity of the characteristic line of $Fe^{3+}$. The $Fe^{3+}/Fe_{tot}$ of the silicate analyzed on this ROI is as low as 38%. The corresponding XRD pattern collected before the NFS analysis shows that the amount of smectite, magnetite and pyrrhotite are lower than in other grains and ROIs (Fig. 5), smectite diffraction lines being absent from the pattern. This spectrum therefore allows us to suggest that among the clay minerals making up most of the silicate fraction of Ryugu, smectite is more oxidized than serpentine. If a precise quantification of the smectite/serpentine ratio was available for several grains, one could certainly provide the characteristic redox states of each of these coexisting phases. This is, to date not amenable, but lower and upper estimates are discussed below.

# 5 Discussion

## *5.1 Comparison with CI chondrites*

One of the most striking early results drawn from Ryugu returned samples is that most of their geochemical signatures are akin to those of CI chondrites (e.g. Ito et al., 2022; E. Nakamura et al., 2022; Yokoyama et al., 2022; Hopp et al., 2022; Moynier et al., 2022; Paquet et al., 2023). The bulk mineralogy of these samples also shares strong similarities with CI material (T. Nakamura et al., 2022; Ito et al., 2022). In this context, Mössbauer spectroscopies grant access to the iron distribution and valence state among the different phases found in Ryugu and then allow us to compare them to CI and CI-like materials. Bland et al. (2004) derived the iron distribution in Orgueil from combined XRD and conventional Mössbauer spectroscopy. Here, we alternatively recalculated the Fe distribution in Ivuna, the most recent fall (1938), which is alleged to be the least terrestrially altered CI chondrite as compared to Orgueil or Alais (King et al., 2015, 2020). Based on these published data, the Fe distribution in Ivuna is roughly 24% in sulfide, 52% in magnetite and 24% in clay minerals. These values are similar to the one obtained by Mössbauer spectroscopy in our study and really close to grain C0061 and significantly differs from Orgueil and Alais. This confirms, indirectly, the robustness of our Mössbauer results and the similarities between the mineralogy of Ryugu samples and CI meteorites.

Nevertheless, significant differences are also seen between the iron mineralogy of Ryugu and CI chondrites based on the sole MS spectra (Fig.11). First, Orgueil and Alais contain significant amount of ferrihydrite (nominally $5Fe_2O_3.9H_2O$) in a superparamagnetic form (Madsen et al., 1986; Tomeoka and Buseck, 1988; Gounelle and Zolensky, 2001; Bland et al., 2004, King et al. 2015). The weight fraction of ferrihydrite does not exceed 5%, yet this represents an Fe amount similar to what is currently accommodated in sulfides and half of the Fe present as magnetite. Because of its superparamagnetic nature, the signal, collected at room temperature, adds up to the typical doublet for $Fe^{3+}$ in silicates. This typically leads to the erroneous view that iron-bearing silicates present in CI chondrites are highly oxidized (Face values derived from typical Mössbauer spectra would lead to $Fe^{3+}/Fe_{tot} > 90\%$, Fig. 11). The nature of this mineral and its origin has been a matter of discussion for years (Wdowiak and Agresti, 1984; Madsen et al., 1986; Tomeoka and Buseck, 1988). But it is now commonly interpreted as one of the consequences of terrestrial alteration of sulfides (Gounelle and

Zolensky, 2001). In Ryugu samples analyzed here, no trace of ferrihydrite was reported by XRD, TEM and spectroscopic analysis (T. Nakamura et al., 2022; Yokoyama et al., 2022; Ito et al., 2022; Viennet et al., 2022). Moreover, it has been recently noted that Ryugu samples contain nanometer-size pyrrhotite embedded in clay minerals that are absent in Orgueil and may represent precursors of the ferrihydrite (T. Nakamura et al., 2022). As expected, without this strong contribution of ferrihydrite, the overall $Fe^{3+}/Fe_{tot}$ derived from non-magnetic Mössbauer lines (generally assigned to silicates) is much lower in Ryugu than in CI materials and $Fe^{3+}/Fe_{tot}$ varies from 38 to 68% (Table 3) against typically > 90% for Orgueil and Alais (Fig. 11). It is however not clear, for now, if the reduced nature of Ryugu's silicates is only due to the lack of ferrihydrite or is also due to an initially more reduced nature of these clays as discussed in more detail below.

A second major difference can be observed between typical MS spectra of Ryugu particles and Orgueil. The relative intensities of the magnetite lines differ (lines at high velocity). In Ryugu samples, the distribution of Fe in the two sites is stoichiometric (1/3 and 2/3) while magnetite in Orgueil is not stoichiometric and appears to be over-oxidized (Madsen et al., 1986). This anomalous redox ratio of the so-called *magnetite* found in Orgueil is attributed to a maghemite component making up for 12 at% of the magnetic component generally assigned to magnetite (Madsen et al., 1989; Gunnlaugsson et al., 1994). This also points to the oxidized nature of CI chondrites recovered on Earth as compared to the Ryugu samples. However, contrary to the presence of ferrihydrite, it is difficult here to unambiguously interpret the occurrence of maghemite in Orgueil as a direct consequence of terrestrial alteration. Nonetheless, we still note that the oxidation of nano- and micro-magnetite in terrestrial samples is a well-known consequence of the high oxygen fugacity of the Earth surface.

Finally, the differences between Ryugu particles and Orgueil in terms of redox state can be summarized by their iron average valence states. It is lower in Ryugu samples (typically between 2.49 and 2.55) than the value derived for Orgueil (2.604, Garenne et al., 2019). We note however that the Orgueil values were derived from a different method (Fe-XANES) that can be sensitive to X-ray induced oxidation in phyllosilicates (Reynard et al. 2022). In addition, the Lamb-Mössbauer factors were not taken into account here. Indeed, the *true* $Fe^{3+}/Fe_{tot}$ of clays may not be strictly proportional to the areas of the quadrupole doublets as tabulated in Table 3. Though generally neglected in the literature, the recoil-free fraction of iron atoms is slightly different for $Fe^{2+}$ and $Fe^{3+}$ in silicates at any temperature. Despite the fact that the correction can vary from a mineral to the other, a typical, reasonable, correction can be

assumed: the ratio of doublet areas for $Fe^{3+}$ and $Fe^{2+}$ can overestimates the *true* $Fe^{3+}/Fe_{tot}$ by a factor of up to 1.2 (De Grave and Van Alboom, 1991; Dyar et al. 2009; Roskosz et al., 2022). The need for such correction on these samples is uncertain and for this reason we did not provide the corrected ratios in Table 3. The difference is still within the typical error associated with redox determination based on Mössbauer spectra, typically estimated to 3-5%.

*5.2 Crystal chemistry and redox state of Fe in serpentines and smectites from Ryugu*

Clay minerals are built from the stacking of tetrahedral (T) and octahedral (O) layers, either as TOT (for 2:1 clay minerals such as smectites) or as TO layers (for 1:1 clay minerals and serpentines). In these minerals, Fe can substitute for Si in the tetrahedral plane only as $Fe^{3+}$ (here after labelled $^{IV}Fe^{3+}$) because its ionic radii is small enough to be accommodated in the tetrahedron, while the ionic radius of $Fe^{2+}$ in four-fold coordination is too large to fit within the lattice (Meunier, 2005). Conversely, both $Fe^{2+}$ or $Fe^{3+}$ in six-fold coordination can be located in the octahedral layer (respectively named here after, $^{VI}Fe^{2+}$ and $^{VI}Fe^{3+}$).

The isomer shift (IS) and the quadrupole splitting (QS) determined from Mössbauer spectra provide key information on the Fe crystal chemistry in clay minerals (Dyar and Sklute, 2019). We note first that $^{VI}Fe^{2+}$ in serpentine has an IS value at around 2.73 $mm.s^{-1}$ while $^{VI}Fe^{3+}$ exhibit IS values ranging from 0.1 to 0.24 $mm.s^{-1}$, with QS values from 0.5 up to 1.0 $mm.s^{-1}$ (Rozenson et al., 1979; Blaauw et al., 1979; Mizutani et al., 1991; Fuch et al., 1998; González-Mancera et al., 2003). Also, $^{IV}Fer^{3+}$ in serpentine has IS values around 0.2 and QS values around 0.34 (Mizutani et al., 1991). For minerals containing 2:1 layers such as smectite, $^{VI}Fe^{2+}$ has IS values ranging from 1.0 $mm.s^{-1}$ to 1.2 $mm.s^{-1}$ with QS values between 0.5 and 2.6 $mm.s^{-1}$ (Fox et al., 2021), while $^{IV}Fe^{3+}$ has IS values ranging from 0.15 to 0.32 $mm.s^{-1}$ with QS values from 0.6 to 0.65 $mm.s^{-1}$ (Baron et al., 2017). In the same minerals, $^{VI}Fe^{3+}$ has IS values ranging from 0.3 to 0.35 with QS from 0.34 up to 1.3 $mm.s^{-1}$ (Baron et al., 2017). The typical IS and QS values obtained on the Ryugu grains are presented (Fig.12) against the typical ranges for IS and QS as reviewed by Dyar and Sklute (2019).

In order to investigate the crystal chemistry of Fe in clay minerals, we will now focus on data obtained under magnetic field (polarized), which typically leads to more robust fits to the data (see above). The IS and QS values for 1:1 and 2:1 clay minerals strongly overlap and consequently, it is not possible to use IS and QS to unambiguously determine the nature and individual properties of clay minerals. However, we used the high spatial resolution of NFS coupled to the heterogeneity of Ryugu samples to disentangle the crystal chemistry of Fe

accommodated in serpentines and in smectites. Ideally, in clay minerals, at least one doublet should be used to describe each contribution of $^{VI}Fe^{3+}$ and $^{IV}Fe^{3+}$ to the Mössbauer spectra (Baron et al., 2017). Yet, as previously discussed, here, only one doublet was used to describe these two contributions because of the complexity of the Fe mineralogy in Ryugu samples. The use of such a single doublet to describe the $Fe^{3+}$ contributions in both tetrahedral and octahedral sheets recently gave satisfying results for synthetic clay minerals (Fox et al., 2021). In such a case, the IS and QS values correspond to an intermediate value between the values describing the two doublets.

Focusing first on grain A0117B, we note that the XRD patterns shows low amount of smectite and relatively high amount of serpentine. The XRD pattern associated to the focused and polarized NFS spectrum shows the same yet exacerbated features: a high content of serpentine and no detectable smectite (Fig. 5). The NFS spectrum is also significantly different from the others (Fig. 7). The fit to the spectrum also shows that the $Fe^{3+}/Fe_{tot}$ and the IS and QS values are significantly different (Fig.12). Based on this NFS spectrum and XRD patterns, we conclude that the typical $Fe^{3+}/Fe_{tot}$ of serpentine is at most ~35%. Furthermore, the IS and QS values lie within the field of $^{IV}Fe^{3+}$ (yet not far from the field of $^{VI}Fe^{3+}$ because in serpentines, $^{IV}Fe^{3+}$ is always associated to $^{VI}Fe^{3+}$ as shown in Rozenson et al., 1979 and in Blaauw et al., 1979). Our results therefore suggest that a significant fraction of $^{IV}Fe^{3+}$ is accommodated in Ryugu's serpentines. This is an unusual coordination in serpentines, where $^{VI}Fe^{3+}$ is more common (González-Mancera et al., 2003 and references therein). Yet, among the serpentine polytype, lizardite is enriched in $^{IV}Fe^{3+}$ as compared to $^{VI}Fe^{3+}$ (O'Hanley and Dyar, 1993). Lizardite is also more akin to accommodate trivalent Fe than chrysotile (Whittaker and Wicks, 1970; Wicks and Whittaker, 1975). In Ryugu and more generally, in CI meteorites, the polytype of serpentine has not been extensively discussed to our knowledge. It is however of note that chrysotile has a tubular structure that is not observed in Ryugu or CI materials. Furthermore, antigorite is the HT/HP polymorph of lizardite and could certainly not form in asteroidal conditions. We therefore suggest that the polytype of serpentine in Ryugu is a relatively reduced lizardite. Recent advanced transmission electron microscopy works also suggest that lizardite is the main polytype in chamber A samples from Ryugu (Bahae-eddine et al., this issue) and therefore are fully in line with our Mössbauer results.

Now, turning to grains A0026 and C0061, the overall $Fe^{3+}/Fe_{tot}$ of clay minerals, the IS and QS values for $Fe^{3+}$ differ from grain A0117B. The XRD patterns of A0026 and C0061 highlight the presence of smectite-rich clay minerals as compared to grain A0117B-focused (Fig.5). The $Fe^{3+}/Fe_{tot}$ is much higher than for A0117B-focused and the IS and QS point toward

647 an $^{VI}Fe^{3+}$-dominated crystal chemistry (based on the study of Baron et al., 2017, for pure
648 nontronite). Since these grains still contain significant amount of serpentine, the characteristic
649 $Fe^{3+}/Fe_{tot}$ of smectite remains unknown but must be higher than 65%, which makes smectite
650 the dominant carrier of ferric iron with magnetite in the Ryugu sample.
651
652 *5.3 Implications on the nature of circulating fluids in the parent body of asteroid Ryugu*
653
654 The Fe-bearing minerals from Ryugu bear multiple information about the physical
655 chemical conditions that presided to their formation. For instance, Ryugu's magnetite records
656 the paleomagnetic field when they precipitated (T. Nakamura et al. 2022; Sato et al. 2022).
657 Similarly, iron coordination chemistry can be used because physical and chemical conditions
658 can either promote or inhibit their accommodation in clay minerals (Mizutani et al., 1991;
659 Andrieux and Petit, 2010; Baron et al., 2016; Dzene et al., 2018; Boumaiza et al., 2020; Dzene
660 et al., 2022). In particular, the substitution of $^{IV}Fe^{3+}$ for $^{IV}Si^{4+}$ is hardly favored during clay
661 mineral formation in aqueous systems. Experimentally, the pH of the solution appears to be the
662 key driving parameter (Baron et al., 2016; Dzene et al., 2018; Boumaiza et al., 2020). A pH >
663 12.5 (for both 1:1 and 2:1 clays) is experimentally required for a significant accommodation of
664 $^{IV}Fe^{3+}$. It is therefore likely that serpentine (and possibly saponite) found in Ryugu (or at least
665 in sample A0117B) formed under basic conditions with pH value even higher than 12.5. The
666 fact that clay minerals formed under basic conditions in CI parent bodies has been known (T.
667 Nakamura et al., 2022), but pH as high as 12.5 have not been discussed so far. Considering the
668 presence of $^{IV}Fe^{3+}$ in thermodynamic models such as the recent one proposed by T. Nakamura
669 et al. (2022) would certainly help to better constrain the geochemical conditions that presided
670 to the aqueous alteration of CI parent bodies.

# 6 Conclusion

We developed an analytical framework to investigate the iron mineralogy and valence state in extraterrestrial materials at the micron-scale by combining X-ray diffraction, conventional Mössbauer and nuclear forward scattering spectroscopies. A relatively large array of standard minerals was studied but this database should grow in the future to make this technique amenable in cosmochemistry. Of particular interest would be an array of clay minerals of different nature and various redox state. Based on these cross-calibration, we collected MS and NFS spectra on three Ryugu grains. We found that iron is essentially accommodated in magnetite, clay-minerals (serpentine-smectite) and sulfides. A single set of Mössbauer parameters were necessary to account for the entire variability observed at the bulk and the spatially-resolved scale. These parameters represent a fully consistent iron mineralogical model for the Ryugu samples. From these analysis, it is concluded that Ryugu grains are overall similar to each other and similar to CI chondrites. In details however, no ferrihydrite was found in Ryugu particles even at the very sensitive scale of Mössbauer spectroscopy. This, in turns, allow for the determination of $Fe^{3+}/Fe_{tot}$ of clay minerals, which was found to be much more reduced than typical redox ratios measured on CI chondrites. Furthermore, magnetite from Ryugu is stoichiometric with no significant maghemite component, whereas up to 12% of maghemite was identified in the magnetic phases measured in Orgueil. It is likely that most of CI meteorites suffered from terrestrial alteration but it is not clear for now if the parent bodies of the CI chondrite were as reduced as Ryugu. The high spatial resolution of NFS was put in use to disentangle the redox state and the crystal-chemistry of iron accommodated in serpentine and smectite. It is found that the polytype of serpentine is likely lizardite, containing less than 35% of $Fe^{3+}$, a fraction of which being tetrahedrally-coordinated. Smectite is more oxidized ($Fe^{3+}/Fe_{tot} > 65\%$) and mainly contains octahedral ferric iron. This finding implies that these clays formed from highly alkaline fluids.

More detailed crystal-chemical analysis of these clays must now be carried out. Recent experimental synthesis of phyllosilicates showed that temperature, kinetics and pH conditions affect the content and the crystallinity of the smectite/serpentine assemblages, smectite being more crystalline and more present at higher pH, shorter precipitation duration and higher temperature (Boumaiza et al., 2020). The various content and crystallinity observed here in Ryugu clay mineral assemblages may indicate that different geochemical conditions of formation are recorded at a very local scale. Moreover, the significant differences between the

redox states of smectite and serpentine could also suggest that redox conditions varied during the formation of each of these phases. This must be confirmed by further NFS analysis and may be consistent with the multiple generations of magnetite identified in Ryugu and interpreted as the fruits of the variable geochemical conditions and/or a formation under non-equilibrium conditions (Dobrică et al., 2023).

.

# 7 Acknowledgement

We thank M. Zolensky for efficient handeling of this manuscript and two anonymous reviewers for positive and thoughtfull suggestions on the initial version of this manuscript. This work was supported by the PICS CNRS project “Meteoredox” granted to MR and PB. It was also supported by the FACCTS grant “Straight Out of the Asteroid Belt to the Inelastic Lines at the Advanced Photon Source” to EEA and MR. Support was also granted by the French “Classy” ANR to MR. Moreover, PB acknowledges funding from the European Research Council (ERC) under the grant SOLARYS ERC-CoG2017-771691. MR and JCV gratefully acknowledge financial support from the Paris Ile-de-France Region DIM ACAV+ funding (PARYUGU) and from the ATM 2022_project “Orgueil” (OE-7590) from MNHN. We finally thank Mizuha Kikuiri and Eiichi Kagawa (Tohoku Univ.) for sample preparation.

# 8 References


Andrieux P., and Petit S. 2010. Hydrothermal synthesis of dioctahedral smectites: The Al–Fe3+ chemical series. *Applied Clay Science* 48:5–17.

Bancroft G. M., Maddock A. G., and Burns R. G. 1967. Applications of the Mössbauer effect to silicate mineralogy—I. Iron silicates of known crystal structure. *Geochimica et Cosmochimica Acta* 31:2219–2246.

Baron F., Petit S., Tertre E., and Decarreau A. 2016. Influence of Aqueous Si and Fe Speciation on Tetrahedral Fe(III) Substitutions in Nontronites: a Clay Synthesis Approach. *Clays and Clay Minerals* 64:230–244.

Baron F., Petit S., Pentrák M., Decarreau A., and Stucki J. W. 2017. Revisiting the nontronite Mössbauer spectra. *American Mineralogist* 102:1501–1515.

Blaauw C., Stroink G., Leiper W., and Zentilli M. 1979. Moessbauer analysis of some Canadian chrysotiles. *The Canadian Mineralogist* 17:713–717.

Bland P. A., Cressey G., and Menzies O. N. 2004. Modal mineralogy of carbonaceous chondrites by X-ray diffraction and Mössbauer spectroscopy. *Meteoritics & Planetary Science* 39:3–16.

Blukis R., Rüffer R., Chumakov A.I., and Harrison R.J. 2017. A high spatial resolution synchrotron Mössbauer study of the Tazewell IIICD and Esquel pallasite meteorites. *Meteoritics & Planetary Science* 52:925–936.

Boumaiza H., Dutournié P., Le Meins J.-M., Limousy L., Brendlé J., Martin C., Michau N., and Dzene L. 2020. Iron-rich clay mineral synthesis using design of experiments approach. *Applied Clay Science* 199:105876.

Brearley A. J. 2006. The Action of Water, in Meteorites and the early solar system, ASU press, 587-624

De Grave E., and Van Alboom A. 1991. Evaluation of ferrous and ferric Mössbauer fractions. *Physics and Chemistry of Minerals* 18:337–342.

DeMeo F. E., Binzel R. P., Slivan S. M., and Bus S. J. 2009. An extension of the Bus asteroid taxonomy into the near-infrared. *Icarus* 202:160–180.

Dobrică E., Le Guillou C., and Brearley A. J. 2019. Aqueous alteration of porous microchondrules in Semarkona: Implications for hydration, oxidation and elemental exchange processes. *Geochimica et Cosmochimica Acta* 244:292–307.

Dobrică E. et al. 2023. Nonequilibrium spherulitic magnetite in the Ryugu samples. *Geochimica et Cosmochimica Acta* 346:65–75.

Drits V. A., and Tchoubar C. 2012. *X-ray diffraction by disordered lamellar structures: Theory and applications to microdivided silicates and carbons*, Springer Science & Business Media.

Dyar M. D. et al. 2009. Spectroscopic characteristics of synthetic olivine: An integrated multi-wavelength and multi-technique approach. *American Mineralogist* 94:883–898.

Dyar M. D., and Sklute E. C. 2019. Mössbauer Spectroscopy: Theory and Laboratory Spectra of Geologic Materials. In *Remote Compositional Analysis*, 1st ed., edited by Bishop J. L., Bell III J. F., and Moersch J. E. Cambridge University Press. pp. 147–167 https://www.cambridge.org/core/product/identifier/9781316888872%23CN-bp-7/type/book_part (Accessed April 19, 2023).

Dzene L., Brendlé J., Limousy L., Dutournié P., Martin C., and Michau N. 2018. Synthesis of iron-rich tri-octahedral clay minerals: A review. *Applied Clay Science* 166:276–287.

Dzene L. et al. 2022. Characterization of Iron-Rich Phyllosilicates Formed at Different Fe/Si Ratios. *Clays and Clay Minerals* 70:580–594.

Fox V. K. et al. 2021. Synthesis and characterization of Fe(III)-Fe(II)-Mg-Al smectite solid solutions and implications for planetary science. *American Mineralogist* 106:964–982.

Fuch R., Linare J., Mellini M., Fuchs Y., and Linares J. 1998. Mössbauer and Infrared Spectrometry of Lizardite 1 T from Monte Fico, Elba. *Physics and Chemistry of Minerals* 26:111–115.

Gaffey M. J., Cloutis E. A., Kelley M. S., Reed K. L., and Gehrels T. 2002. Mineralogy of Asteroids. In *Asteroids III*, edited by Bottke W. F., Cellino A., Paolicchi P., and Binzel R. P. University of Arizona Press. pp. 183–204 http://www.jstor.org/stable/j.ctv1v7zdn4.20 (Accessed May 15, 2023).

Garenne A., Beck P., Montes-Hernandez G., Bonal L., Quirico E., Proux O., and Hazemann J. L. 2019. The iron record of asteroidal processes in carbonaceous chondrites. *Meteoritics & Planetary Science* 54:2652–2665.

González-Mancera G., Ortega-Gutiérrez F., Nava N. E., and Arriola H. S. 2003. Mössbauer Study of Serpentine Minerals in the Ultramafic Body of Tehuitzingo, Southern Mexico. *Hyperfine Interactions* 148/149:61–71.

Gounelle M., and Zolensky M. E. 2001. A terrestrial origin for sulfate veins in CI1 chondrites. *Meteoritics & Planetary Science* 36:1321–1329.

Gunnlaugsson H. P., Koch C. B., and Madsen M. B. 1994. Application of external magnetic field to characterize magnetic oxides in the carbonaceous chondrite Orgueil. *Hyperfine Interactions* 91:589–593.

Hastings J. B., Siddons D. P., Van Bürck U., Hollatz R., and Bergmann U. 1991. Mössbauer spectroscopy using synchrotron radiation. *Physical review letters* 66:770.

Herd C. D. K. et al. 2011. Origin and Evolution of Prebiotic Organic Matter As Inferred from the Tagish Lake Meteorite. *Science* 332:1304–1307.

Ito M. et al. 2022. A pristine record of outer Solar System materials from asteroid Ryugu's returned sample. *Nature Astronomy* 6:1163–1171.

Jeandey C., Oddou J. L., Mattei J. L., and Fillion G. 1991. Mössbauer investigation of the pyrrhotite at low temperature. *Solid State Communications* 78:195–198.

King A. J., Schofield P. F., Howard K. T., and Russell S. S. 2015. Modal mineralogy of CI and CI-like chondrites by X-ray diffraction. *Geochimica et Cosmochimica Acta* 165:148–160.

King A. J., Phillips K. J. H., Strekopytov S., Vita-Finzi C., and Russell S. S. 2020. Terrestrial modification of the Ivuna meteorite and a reassessment of the chemical composition of the CI type specimen. *Geochimica et Cosmochimica Acta* 268:73–89.

Krot A. N., Keil K., Scott E. R. D., Goodrich C. A., and Weisberg M. K. 2014. Classification of Meteorites and Their Genetic Relationships. In *Treatise on Geochemistry*. Elsevier. pp. 1–63 https://linkinghub.elsevier.com/retrieve/pii/B9780080959757001029 (Accessed February 25, 2023).

Leroux H., Roskosz M. and Jacob D. 2009 Oxidation state of iron and extensive redistribution of sulfur in thermally modified Stardust particles. *Geochimica et Cosmochimica Acta*, 73, 767-777.

Madsen M. B., Mørup S., Costa T. V. V., Knudsen J. M., and Olsen M. 1986. Superparamagnetic component in the Orgueil meteorite and Mössbauer spectroscopy studies in applied magnetic fields. *Nature* 321:501–503.

Madsen M. B., Mørup S., and Knudsen J. M. 1989. Extraterrestrial magnetite studied by Mössbauer spectroscopy. *Hyperfine Interactions* 50:659–665.

Mahlke M., Carry B., and Mattei P.-A. 2022. Asteroid taxonomy from cluster analysis of spectrometry and albedo. *Astronomy & Astrophysics* 665:A26.

Meunier A. 2005. *Clays*, New York: Springer-Verlag Berlin Heidelberg.

Mizutani T., Fukushima Y., Okada A., Kamigaito O., and Kobayashi T. 1991. Synthesis of 1:1 And 2:1 Iron Phyllosilicates and Characterization of Their Iron State by Mössbauer Spectroscopy. *Clays and Clay Minerals* 39:381–386.

Nakamura T. et al. 2022. Formation and evolution of carbonaceous asteroid Ryugu: Direct evidence from returned samples. *Science* 6:214–220.

Nakamura T. 2005. Post-hydration thermal metamorphism of carbonaceous chondrites. Journal of Mineralogical and Petrological Sciences 100:260–272.

Noguchi et al. 2022. A dehydrated space-weathered skin cloaking the hydrated interior of Ryugu. *Nature Astronomy* 7:170-181.

O'Hanley D. S., and Dyar M. D. 1993. The composition of lizardite 1T and the formation of magnetite in serpentinites. *American Mineralogist* 78:391–404.

Okazaki R. et al. 2022. Noble gases and nitrogen in samples of asteroid Ryugu record its volatile sources and recent surface evolution. *Science* 379:eabo0431.

Prescher C., and Prakapenka V. B. 2015. DIOPTAS: a program for reduction of two-dimensional X-ray diffraction data and data exploration. *High Pressure Research* 35:223–230.

Reynard B., Fellah C., and McCammon C. 2022. Iron oxidation state in serpentines and magnesian chlorites of subduction-related rocks. *European Journal of Mineralogy* 34:645–656.

Roskosz M., Leroux H., Watson H.C. 2008. Thermal history, partial preservation and sampling bias recorded by Stardust cometary grains during their capture. *Earth and Planetary Science Letters*, 273, 195-202.

Roskosz M. et al. 2022. Structural, redox and isotopic behaviors of iron in geological silicate glasses: A NRIXS study of Lamb-Mössbauer factors and force constants. *Geochimica et Cosmochimica Acta* 321:184–205.

Rozenson I., Bauminger E. R., and Heller-Kallai L. 1979. Moessbauer spectra of iron in 1:1 phyllosilicates. *American Mineralogist* 64:893–901.

Rudra A., and Hirschmann M. M. 2022. $Fe^{3+}$ partitioning between clinopyroxene and silicate melt at 1-2.5 GPa: Implications for $Fe^{3+}$ content of MORB and OIB source mantle. *Geochimica et Cosmochimica Acta* 328:258-279.

Shvyd'ko Y. V. 1999. Nuclear resonant forward scattering of x rays: Time and space picture. *Physical Review B* 59:9132.

Sturhahn W. 2000. CONUSS and PHOENIX: Evaluation of nuclear resonant scattering data. *Hyperfine Interactions* 125:149–172.

Sturhahn W. 2004. Nuclear resonant spectroscopy. *Journal of Physics: Condensed Matter* 16:S497–S530.

Sturhahn W., and Jackson J. M. 2007. Geophysical applications of nuclear resonant spectroscopy. In *Advances in High-Pressure Mineralogy*. Geological Society of America https://pubs.geoscienceworld.org/books/book/582/chapter/3803717 (Accessed May 15, 2023).

Tachibana S. et al. 2022. Pebbles and sand on asteroid (162173) Ryugu: In situ observation and particles returned to Earth. *Science* 375:1011–1016.

Tomeoka K., and Buseck P. R. 1988. Matrix mineralogy of the Orgueil CI carbonaceous chondrite. *Geochimica et Cosmochimica Acta* 52:1627–1640.

Vernazza P., and Beck P. 2017. Composition of Solar System Small Bodies. In *Planetesimals: Early Differentiation and Consequences for Planets*, edited by Weiss B. P., and Elkins-Tanton L. T. Cambridge: Cambridge University Press. pp. 269–297 https://www.cambridge.org/core/books/planetesimals/composition-of-solar-system-small-bodies/21A04D349FFBB767D649539E4920431B.

Viennet J.-C. et al. 2023. Interaction between clay minerals and organics in asteroid Ryugu. *Geochemical Perspectives Letters* 25:8–12.

Vilas F. 1994. A Cheaper, Faster, Better Way to Detect Water of Hydration on Solar System Bodies. *Icarus* 111:456–467.

Wdowiak T. J., and Agresti D. G. 1984. Presence of a superparamagnetic component in the Orgueil meteorite. *Nature* 311:140–142.

Whittaker E. J. W., and Wicks F. J. 1970. Chemical differences among the serpentine "polymorphs": a discussion. *American Mineralogist* 55:1025–1047.

Wicks F. J., and Whittaker E. J. W. 1975. A reappraisal of the structures of the serpentine minerals. *The Canadian Mineralogist* 13:227–243.

Yokoyama T. et al. 2022. Samples returned from the asteroid Ryugu are similar to Ivuna-type carbonaceous meteorites. *Science* eabn7850.

Zhang L., Cocco D., Kelez N., Morton D. S., Srinivasan V., and Stefan P. M. 2015. Optimizing X-ray mirror thermal performance using matched profile cooling. *Journal of Synchrotron Radiation* 22:1170–1181.

# Tables

**Table 1: List of standard materials and meteorites analyzed in this study.**

**Table 2: Mössbauer and nuclear forward scattering parameters derived from spectra collected on mineral standards and reference meteorites. IS = Isomer Shift (mm/s), QS = Quadrupole Splitting (mm/s), HT = magnetic hyperfine splitting (T). The typical error associated to each of these parameters is 2% (1σ) for the surface area fractions, of the order of 0.1mm/s for IS and QS and 0.1T for HT. No correction for the Lamb-Mössbauer factors of ferrous and ferric iron in augite, serpentine, chrysotile and smectite was applied (see the discussion for more details about this factor).**

**Table 3: Mössbauer parameters derived from adjusting models to NFS and MS spectra collected on Ryugu grains. IS = Isomer Shift (mm/s), QS = Quadrupole Splitting (mm/s), HT = magnetic hyperfine splitting (T). The typical error associated to each of these parameters is 2% (1σ) for the surface area fractions, of the order of 0.1mm/s for IS and QS and 0.1T for HT. No correction for the Lamb-Mössbauer factors of ferrous and ferric iron in silicates was applied (see the discussion for more details about this factor).**

# Figure Captions

**Fig. 1: (a) Reciprocal properties of radioactive sources and synchrotron radiation lead to reciprocal experimental techniques. Schematically, the quadrupole splitting (QS or Δ) represents in MS spectra, the width of the gap between the two typical dips observed when iron atoms are present in a single crystal site and a single valence state. In NFS spectra, the period of the oscillation is given by 2h/Δ, where h is the Planck's constant (redrawn from Jackson, 2010). (b) Schematic views of the experimental setup and the signal collection process at APS (Argonne National lab, USA).**

**Fig. 2: Nuclear forward scattering spectra (NFS, top panels) and conventional Mössbauer spectra (MS, Middle panels) of anhydrous silicate. The fayalite MS spectrum can be described with two doublets (green and blue lines) both corresponding to $Fe^{2+}$. Conversely, though the augite MS spectrum also needs two doublets, the blue line corresponds to $Fe^{3+}$ and the green line to $Fe^{2+}$ (see Table 2). The three bottom panels are a comparison between the energy-domain spectrum calculated using parameters obtained from NFS and MS.**

**Fig. 3: Nuclear forward scattering spectra (NFS, top panels) and conventional Mössbauer spectra (MS, Middle panels) of hydrous silicate. The chrysotile MS spectrum can be described with two doublets (green and blue lines). The blue line corresponds to $Fe^{3+}$ and the green line to $Fe^{2+}$ (see Table 2). The serpentine MS was described with 2 lines typically assigned to $Fe^{3+}$. The three bottom panels are a comparison between the energy-domain calculated spectrum using parameters obtained NFS and MS.**

**Fig. 4: An example of the effect of an applied external magnetic field on the NSF spectrum of a sample from the magnetite-rich meteorite Tagish Lake.**

**Fig. 5: XRD patterns collected on three different grains, namely C0061, A0026 and A0117B. Left panel: Whole XRD patterns showing the global mineralogy and variations among grains and focused position on grain A0117B. Right Panel: zooms of the XRD patterns on the 001 reflection of clay minerals exhibiting differences in crystallinity/proportion between the different grains.**

**Fig. 6: Conventional Mössbauer spectra of the three Ryugu particles. The fit to the data is the sum of seven different lines shown individually as solid lines.**

**Fig. 7: The NFS spectra collected on three different grains, namely C0061, A0026 and A0117B. Spectra collected on C0061 and A0026 are unfocussed and therefore are representative of the entire grains. Spectra collected on A0117B are focused and document the mineralogy of some selected regions of interest. Both polarized (grey) and unpolarized (red) spectra were collected. The best fits to the data are shown as solid lines on each spectrum and fitting parameters are displayed in Table 3.**

**Fig. 8: Mössbauer parameters derived from analysis of NFS and MS data. Grey symbols are used when derived values derived for all samples for one given site are statistically undistinguishable.**

**Fig. 9: Left panel: $Fe^{3+}/Fe_{tot}$ ratio in the clay minerals derived from analysis of MS and NFS data, as well as the proportion of A and B sites in magnetite. Right panel: fraction of iron in each of the three mineral phases. Horizontal bars are guide for the eyes. Their thicknesses correspond to the typical uncertainty associated to the parameter of interest.**

**Fig. 10: The limited lateral variability in A0026 and C0061 as seen through NFS focused spectra. The numbers relate to different ROIs on the particle.**

**Fig. 11: Comparison of conventional Mössbauer spectra of Ryugu (C0061) and the CI chondrites Orgueil and Alais.**

**Fig. 12: Isomer shift as a function of quadrupole splitting for the polarized measurements of the grains C0061 (unfocussed), A0026 (unfocused) and A0117B (focused). The typical assignments of iron environment ($^{VI}Fe^{2+}$, $^{VI}Fe^{3+}$, and $^{IV}Fe^{3+}$) as a function of IS and QS values were taken from Dyar and Sklute (2019).**

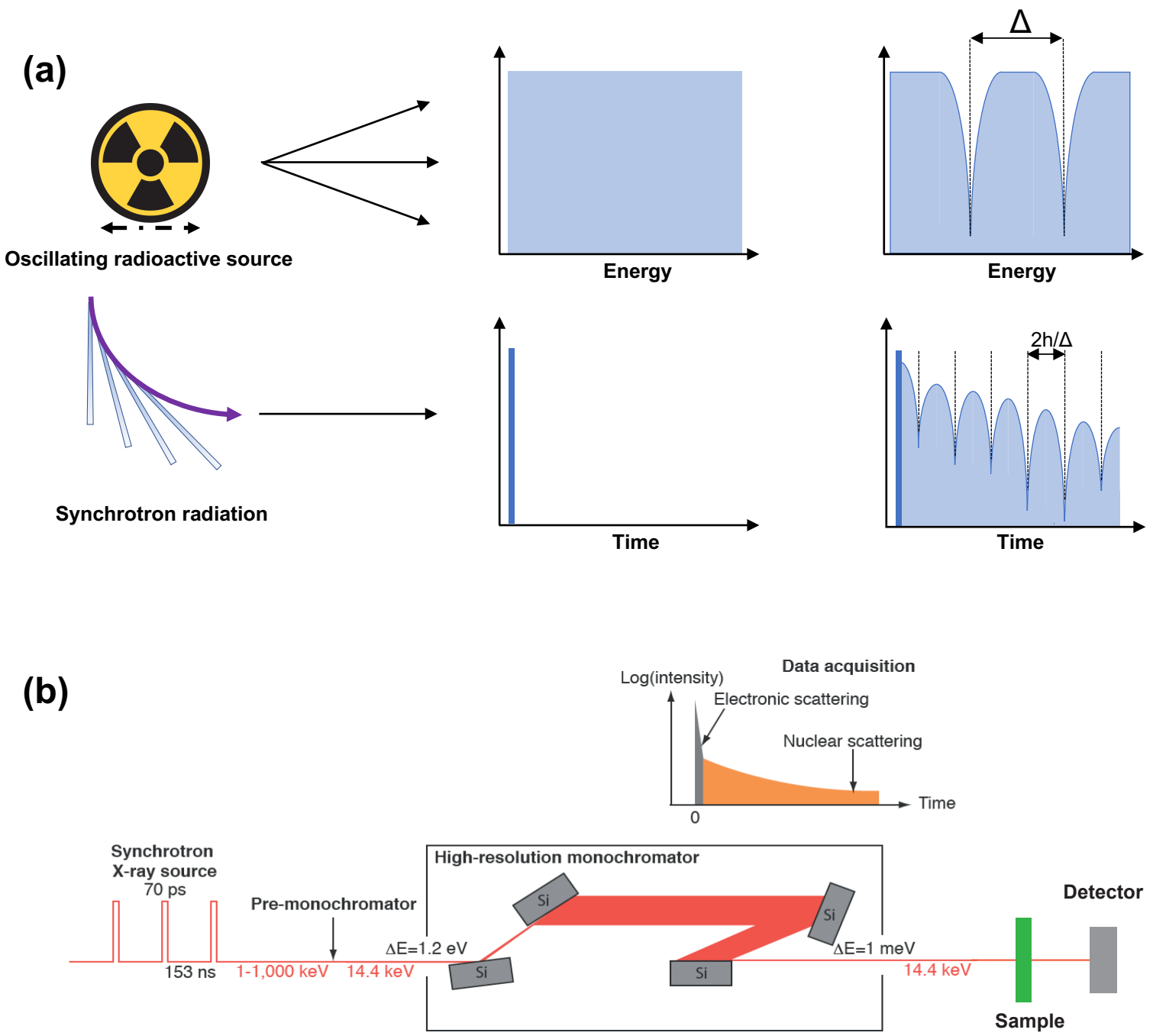
(a)
Oscillating radioactive source
Energy
Δ
Energy
Synchrotron radiation
Time
2h/Δ
Time
(b)
Data acquisition
Log(intensity)
Electronic scattering
Nuclear scattering
Time
0
Synchrotron
X-ray source
70 ps
153 ns
Pre-monochromator
1-1,000 keV
14.4 keV
High-resolution monochromator
Si
Si
Si
Si
ΔE=1.2 eV
ΔE=1 meV
14.4 keV
Detector
Sample

San Carlos

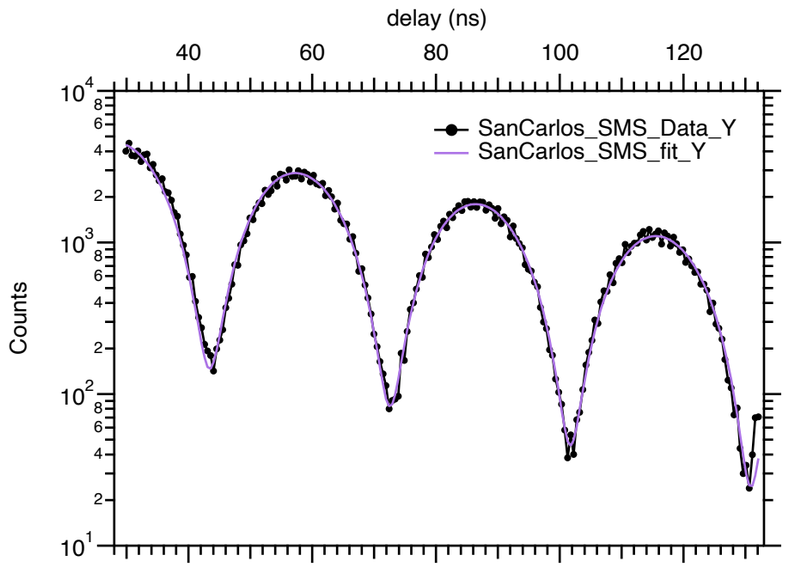


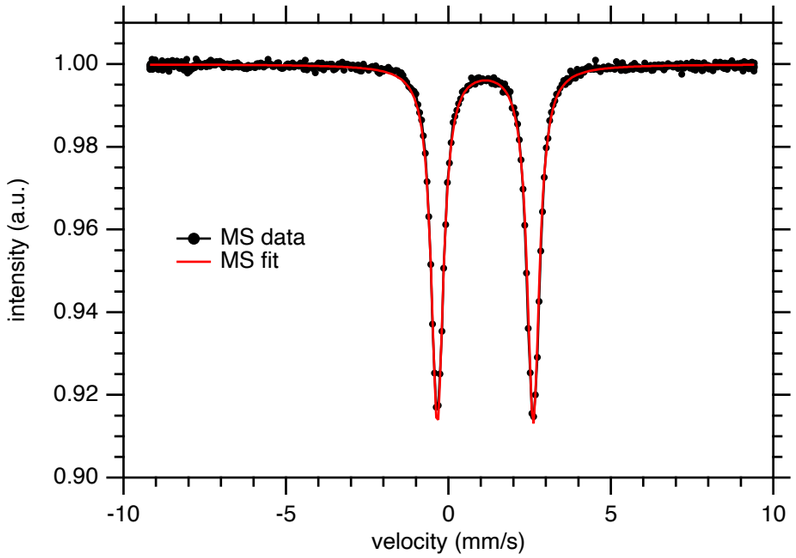


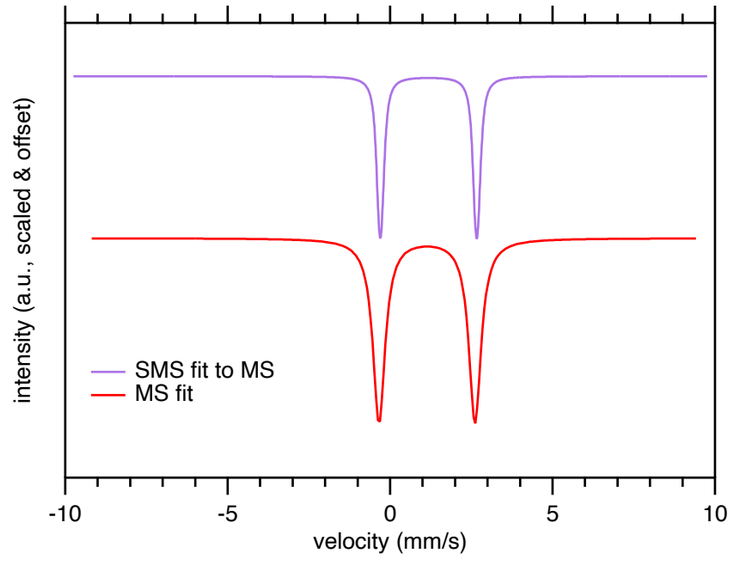


Fayalite

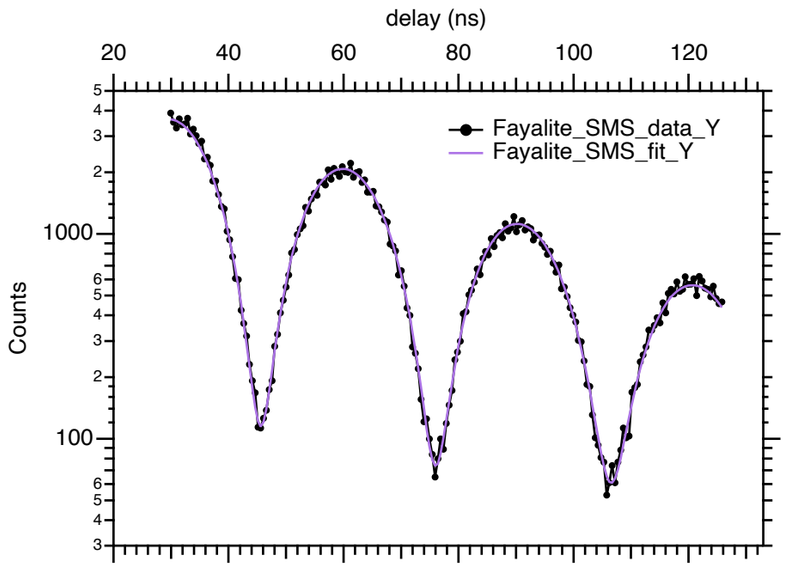


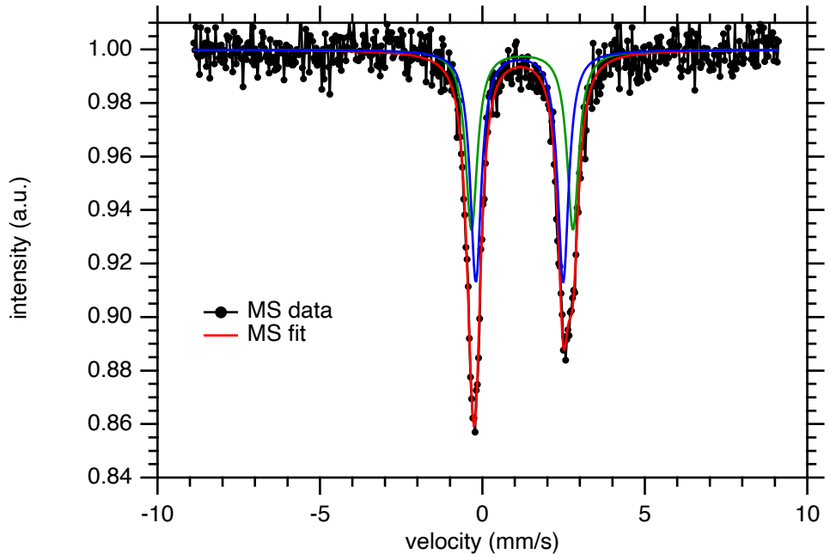


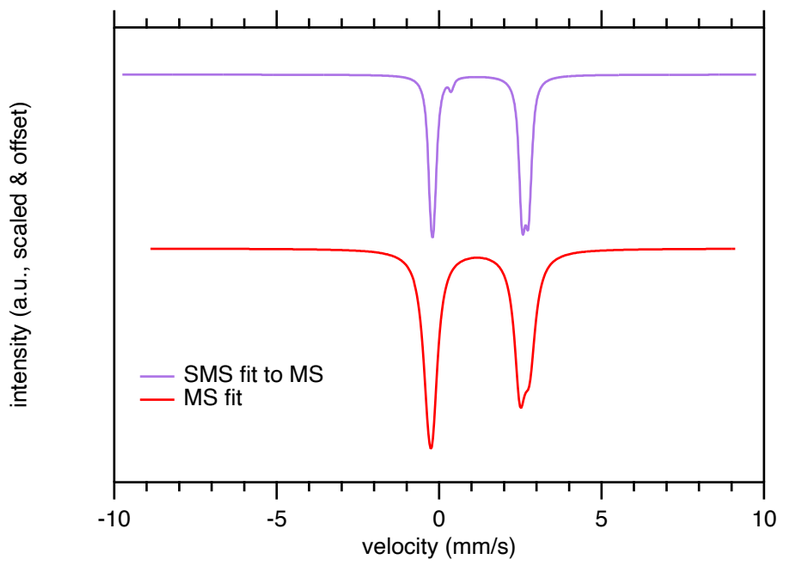


Augite

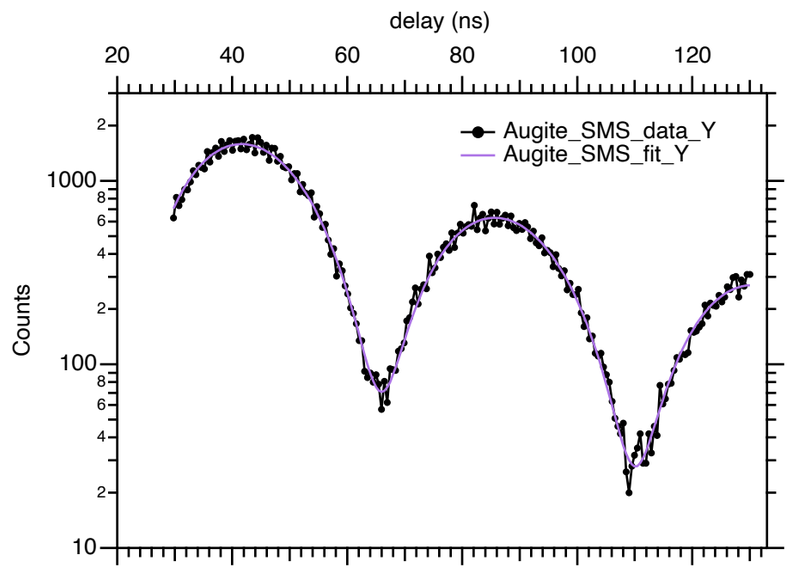


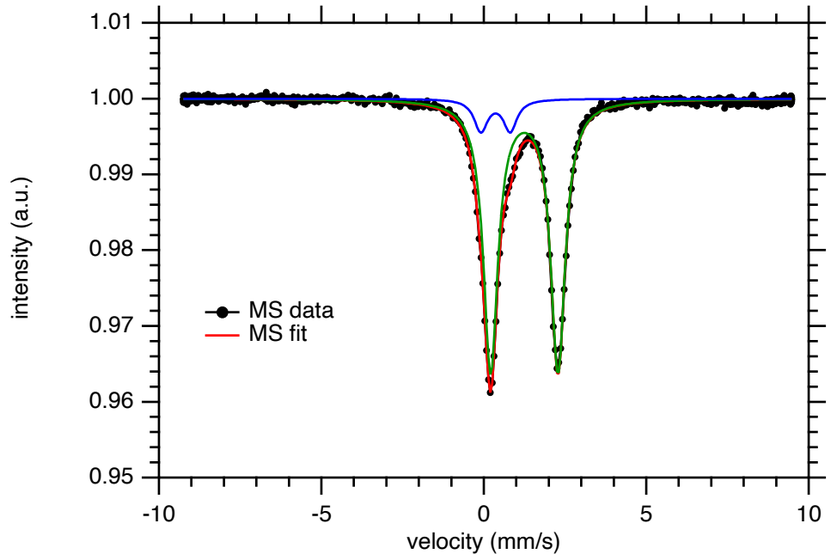


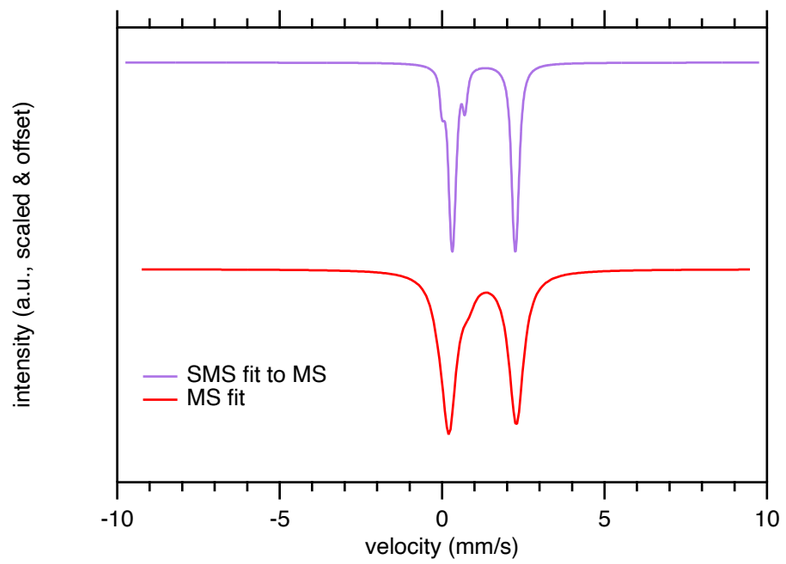

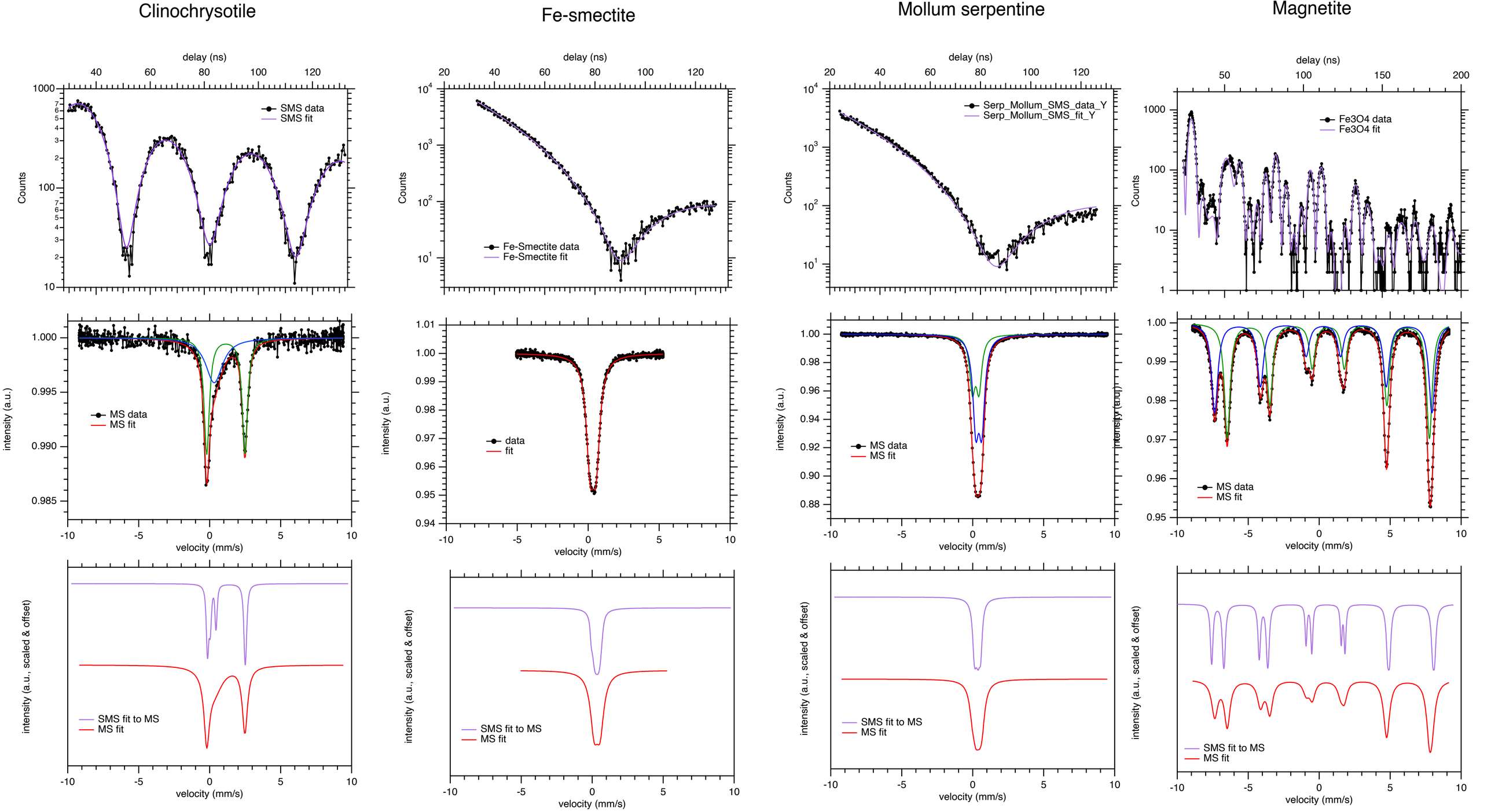
Clinochrysotile
Fe-smectite
Mollum serpentine
Magnetite
delay (ns)
Counts
SMS data
SMS fit
Fe-Smectite data
Fe-Smectite fit
Serp_Mollum_SMS_data_Y
Serp_Mollum_SMS_fit_Y
Fe3O4 data
Fe3O4 fit
intensity (a.u.)
MS data
MS fit
data
fit
velocity (mm/s)
intensity (a.u., scaled & offset)
SMS fit to MS
MS fit

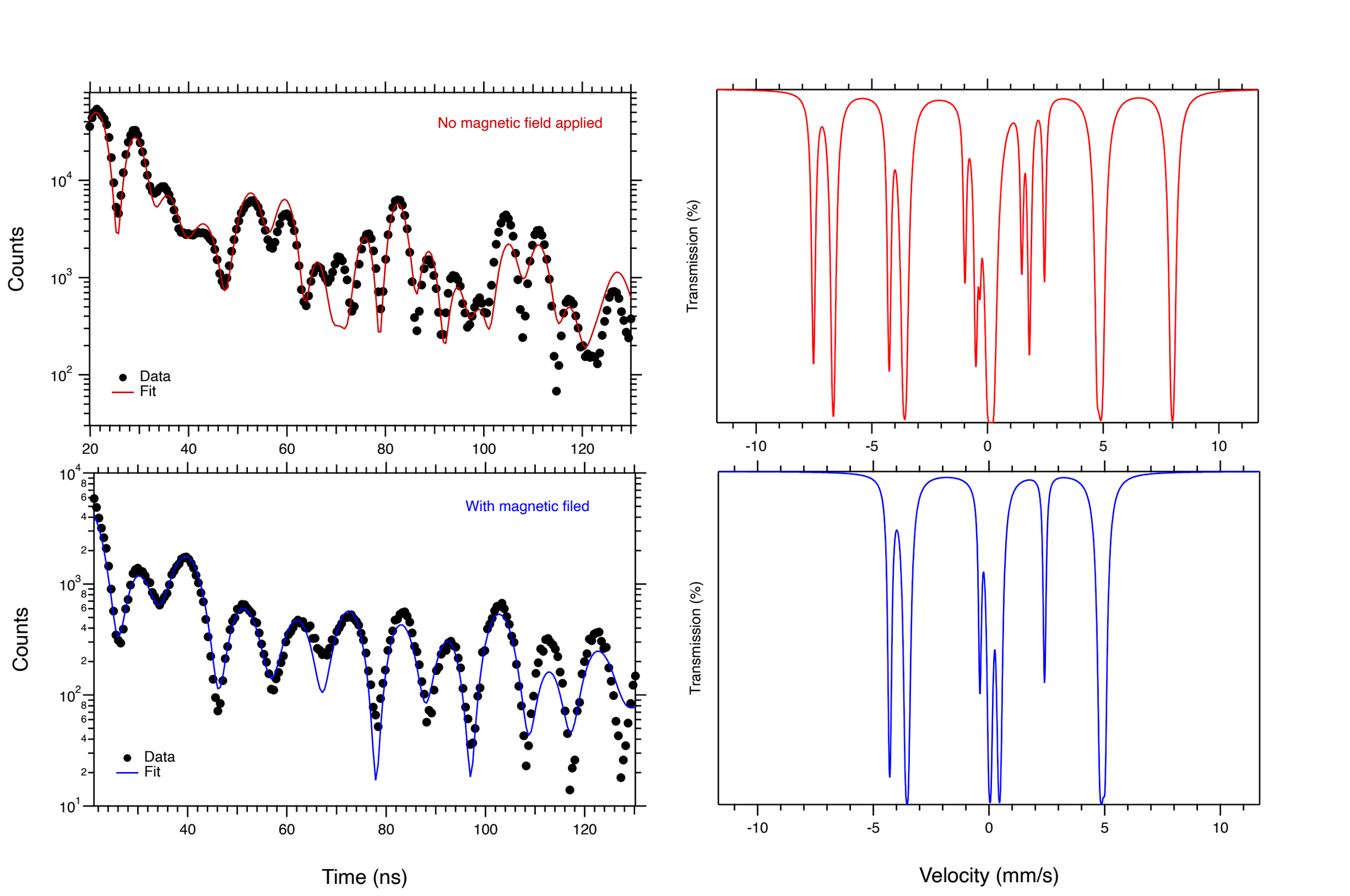
No magnetic field applied
Data
Fit
Counts
With magnetic filed
Data
Fit
Counts
Time (ns)
Transmission (%)
Transmission (%)
Velocity (mm/s)

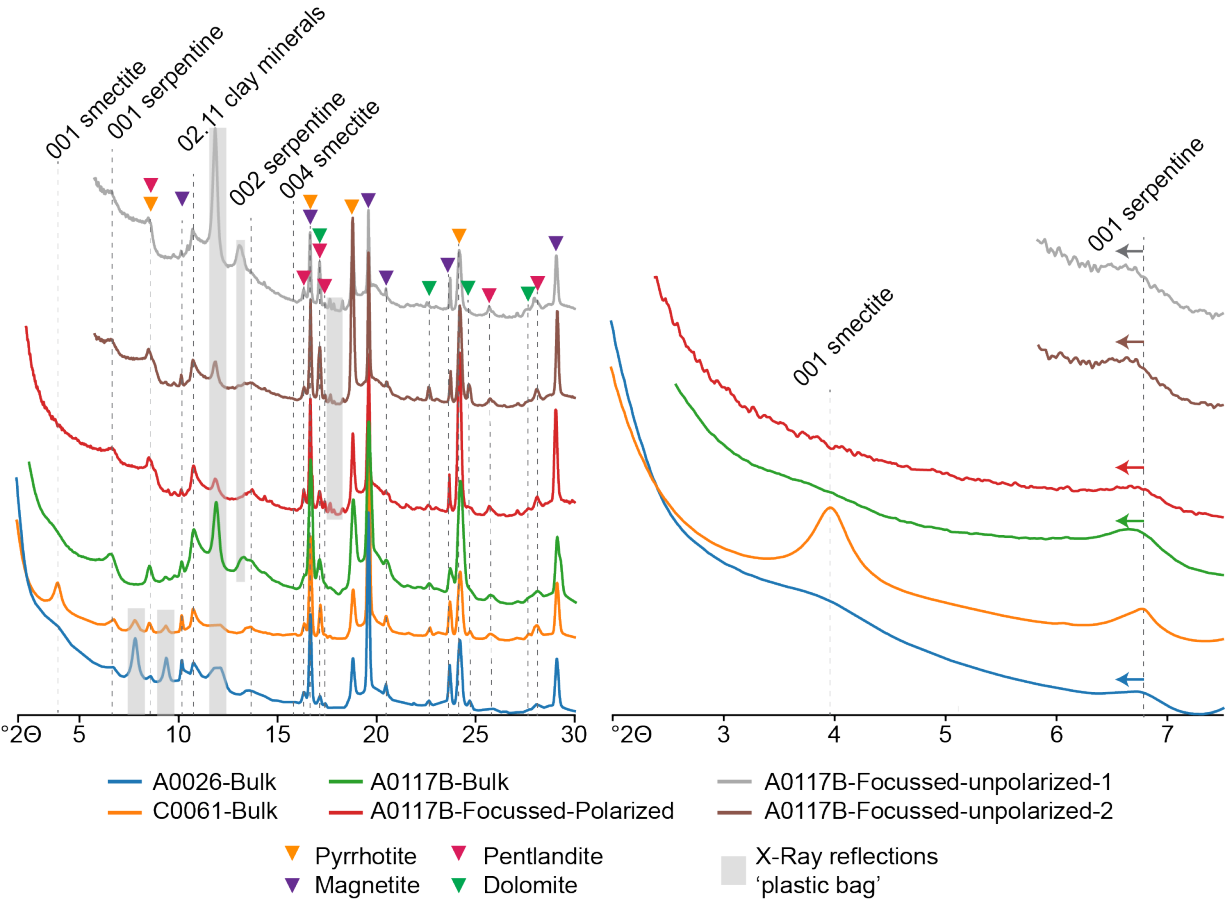
001 smectite
001 serpentine
02.11 clay minerals
002 serpentine
004 smectite
°2Θ
5
10
15
20
25
30
001 smectite
001 serpentine
°2Θ
3
4
5
6
7
A0026-Bulk
C0061-Bulk
A0117B-Bulk
A0117B-Focussed-Polarized
A0117B-Focussed-unpolarized-1
A0117B-Focussed-unpolarized-2
Pyrrhotite
Magnetite
Pentlandite
Dolomite
X-Ray reflections
'plastic bag'

Absorption

1.004
1.002
1.000
0.998
0.996
0.994

Magnetite
Pyrrhotite
Clay
($Fe^{2+}$ - $Fe^{3+}$)
Data
Fit

Hayabusa2
A0026

1.010
1.005
1.000
0.995
0.990
0.985

Magnetite
Pyrrhotite
Clay
($Fe^{2+}$ - $Fe^{3+}$)
Data
Fit

Hayabusa2
A0117

1.03
1.02
1.01
1.00
0.99
0.98
0.97

Magnetite
Pyrrhotite
Clay
($Fe^{2+}$ - $Fe^{3+}$)
Data
Fit

Hayabusa2
C0061

-10
-5
0
5
10
15

Velocity (mm/s)

A0117B

Counts

$10^5$

$10^4$

$10^3$

Magnetic field applied

40 60 80 100 120

Time (ns)

C0061

Counts

$10^5$

$10^4$

$10^3$

$10^2$

Magnetic field applied

40 60 80 100 120

Time (ns)

A0026

Counts

$10^5$

$10^4$

$10^3$

$10^2$

Magnetic field applied

40 60 80 100 120

Time (ns)

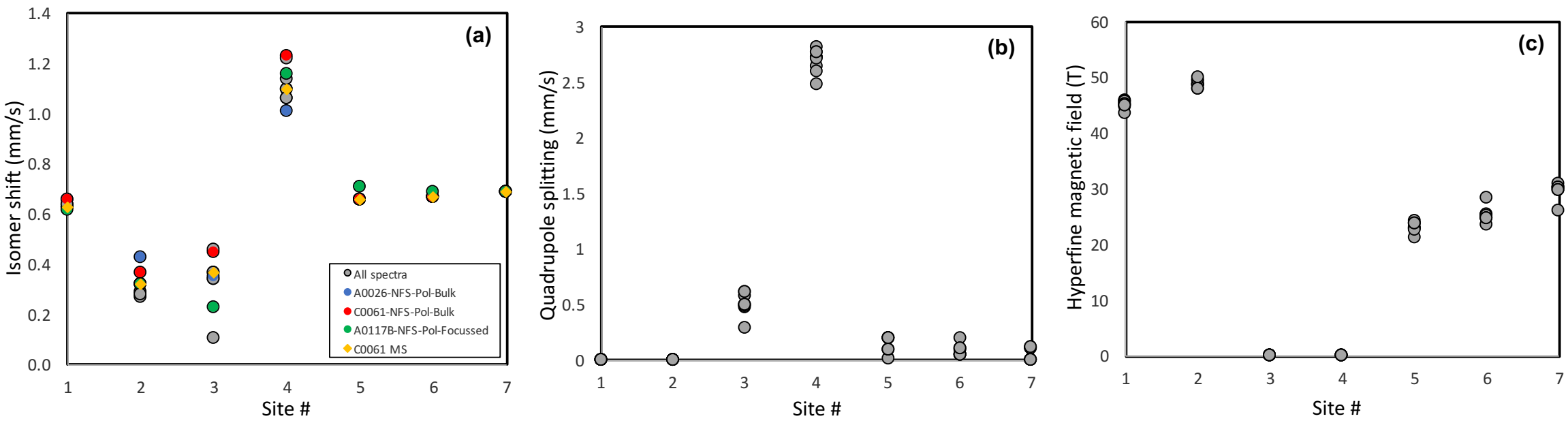
(a)
Isomer shift (mm/s)
Site #
All spectra
A0026-NFS-Pol-Bulk
C0061-NFS-Pol-Bulk
A0117B-NFS-Pol-Focussed
C0061 MS
(b)
Quadrupole splitting (mm/s)
Site #
(c)
Hyperfine magnetic field (T)
Site #

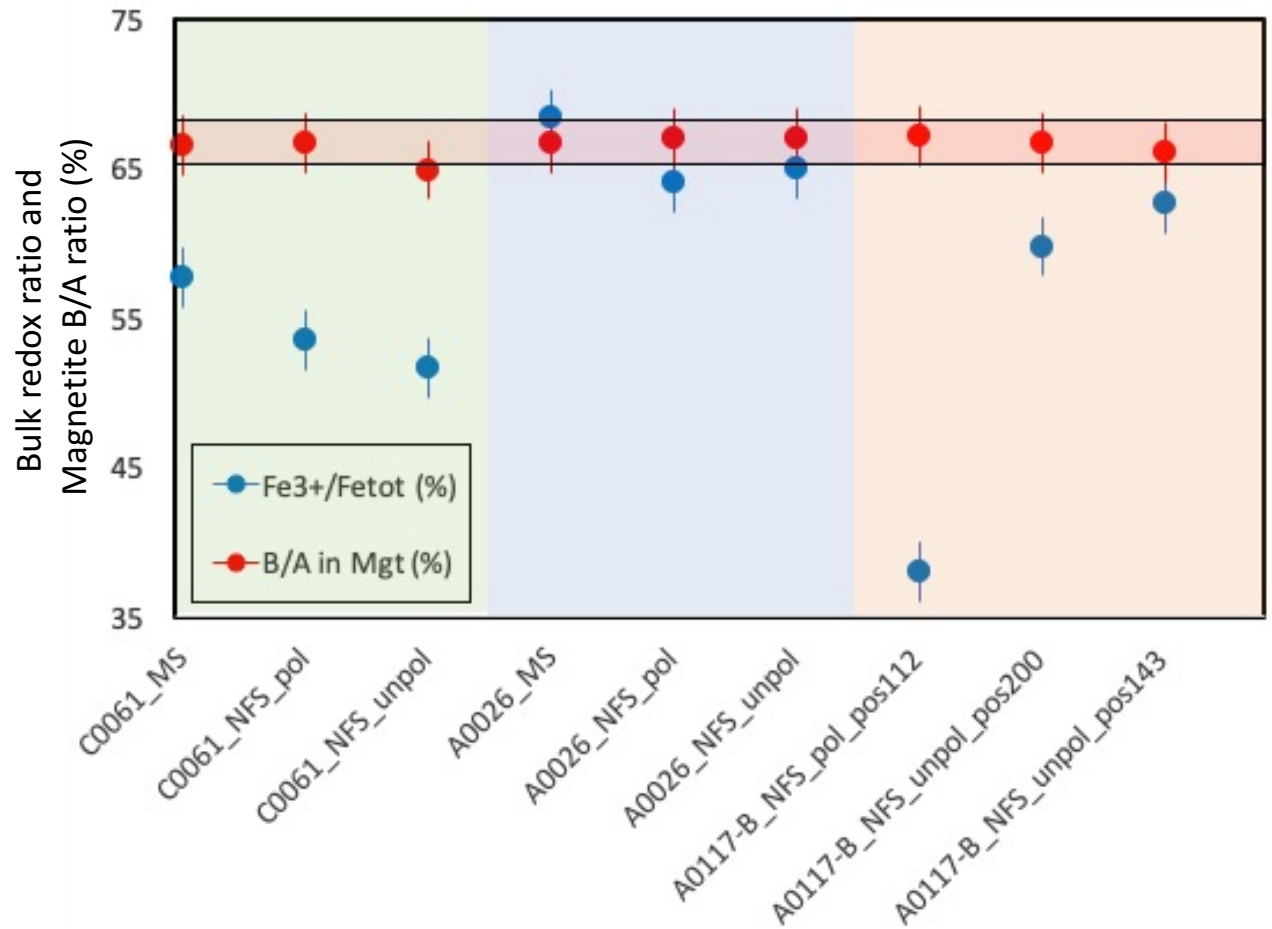
Bulk redox ratio and
Magnetite B/A ratio (%)
75
65
55
45
35
Fe3+/Fetot (%)
B/A in Mgt (%)
C0061_MS
C0061_NFS_pol
C0061_NFS_unpol
A0026_MS
A0026_NFS_pol
A0026_NFS_unpol
A0117-B_NFS_pol_pos112
A0117-B_NFS_unpol_pos200
A0117-B_NFS_unpol_pos143

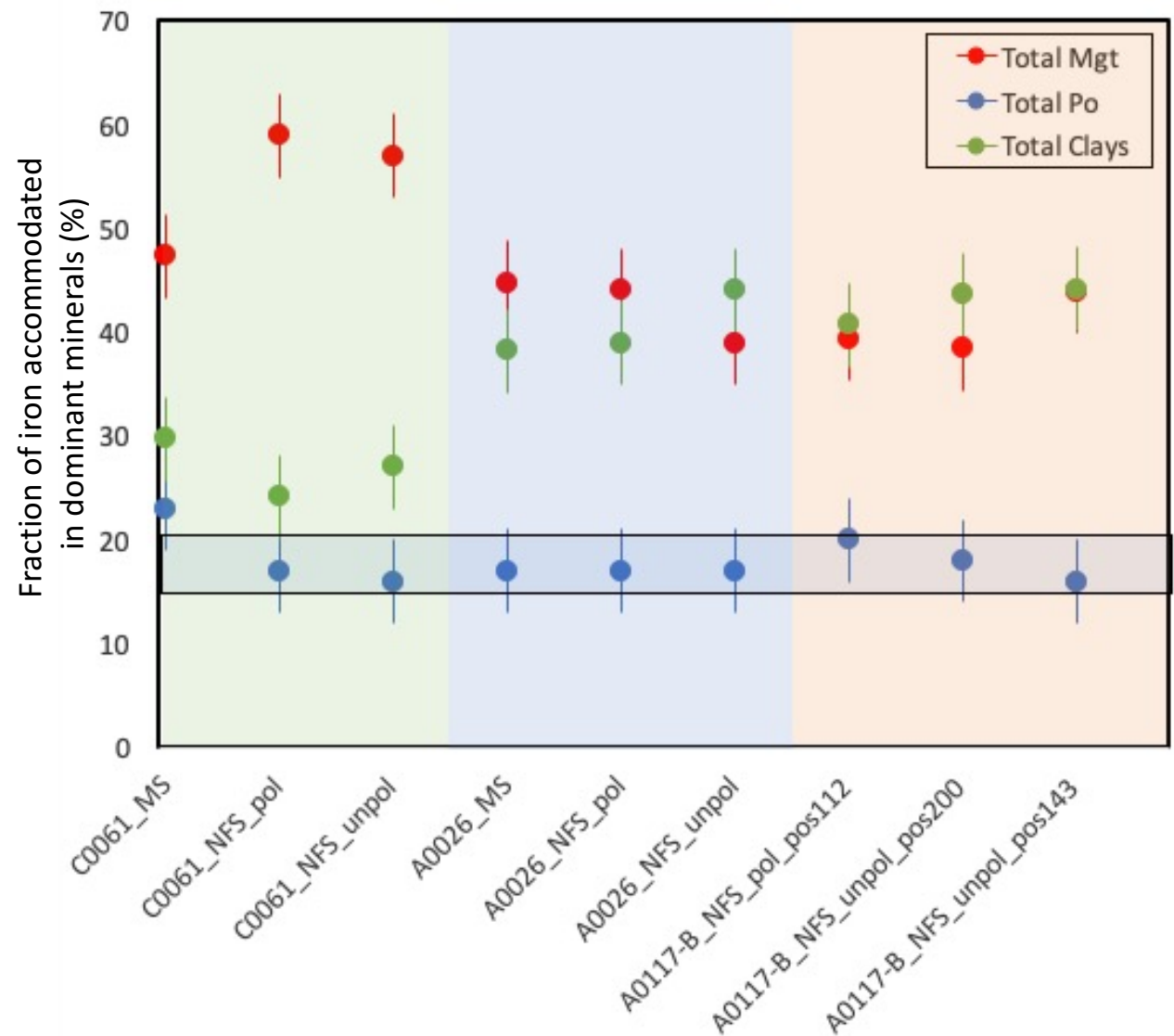
Fraction of iron accommodated
in dominant minerals (%)
70
60
50
40
30
20
10
0
Total Mgt
Total Po
Total Clays
C0061_MS
C0061_NFS_pol
C0061_NFS_unpol
A0026_MS
A0026_NFS_pol
A0026_NFS_unpol
A0117-B_NFS_pol_pos112
A0117-B_NFS_unpol_pos200
A0117-B_NFS_unpol_pos143

A0026

Unfocused

6

5

4

3

2

1

Focused

$10^{10}$ $10^{9}$ $10^{8}$ $10^{7}$ $10^{6}$ $10^{5}$ $10^{4}$ $10^{3}$ $10^{2}$ $10^{1}$ $10^{0}$

40 60 80 100 120

Delay (ns)

C0061

Unfocused

8

7

6

5

4

3

2

1

Focused

$10^{12}$ $10^{11}$ $10^{10}$ $10^{9}$ $10^{8}$ $10^{7}$ $10^{6}$ $10^{5}$ $10^{4}$ $10^{3}$ $10^{2}$ $10^{1}$

40 60 80 100 120

Delay (ns)

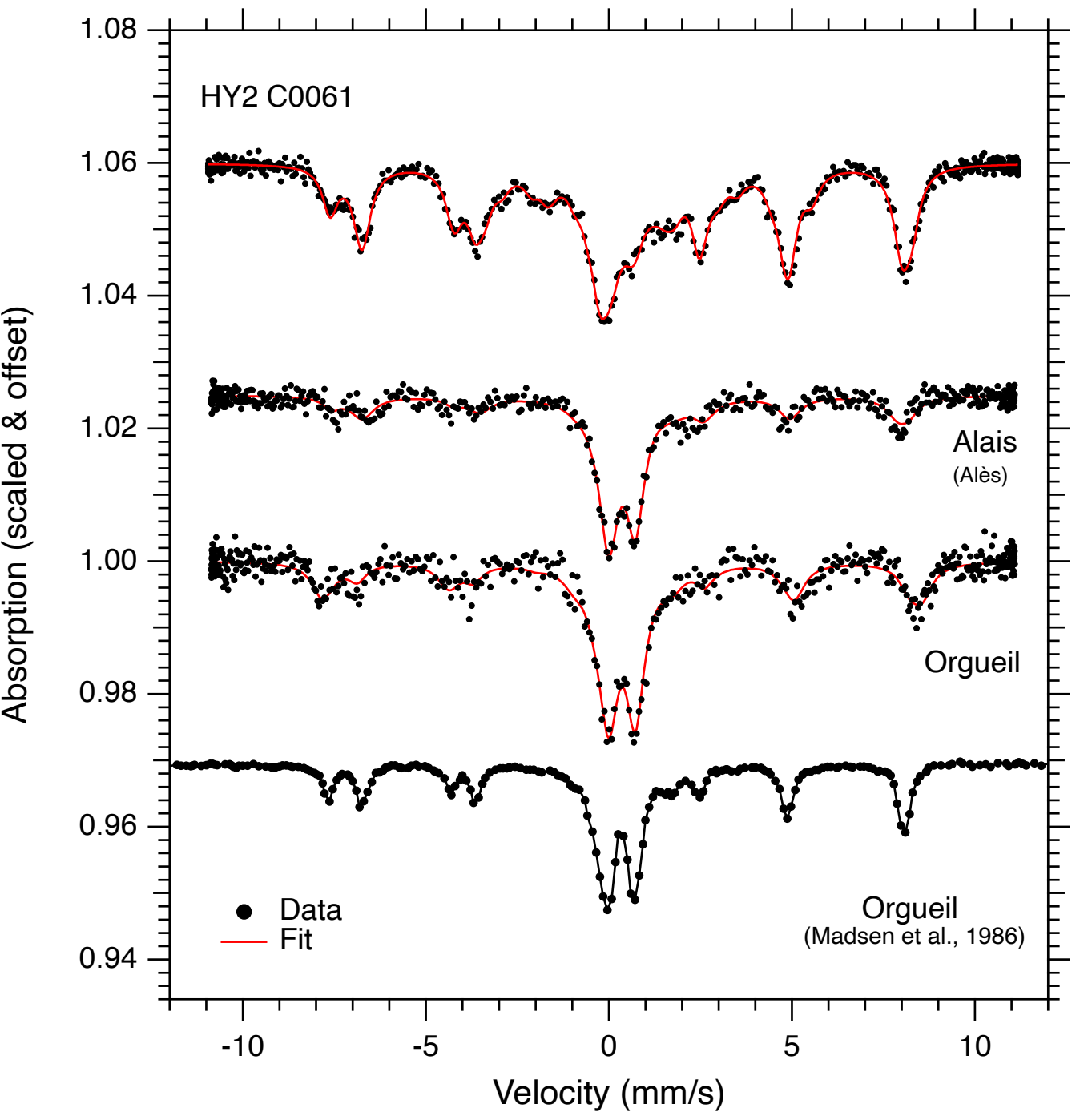
HY2 C0061
Alais
(Alès)
Orgueil
Orgueil
(Madsen et al., 1986)
Data
Fit
Absorption (scaled & offset)
Velocity (mm/s)
1.08
1.06
1.04
1.02
1.00
0.98
0.96
0.94
-10
-5
0
5
10

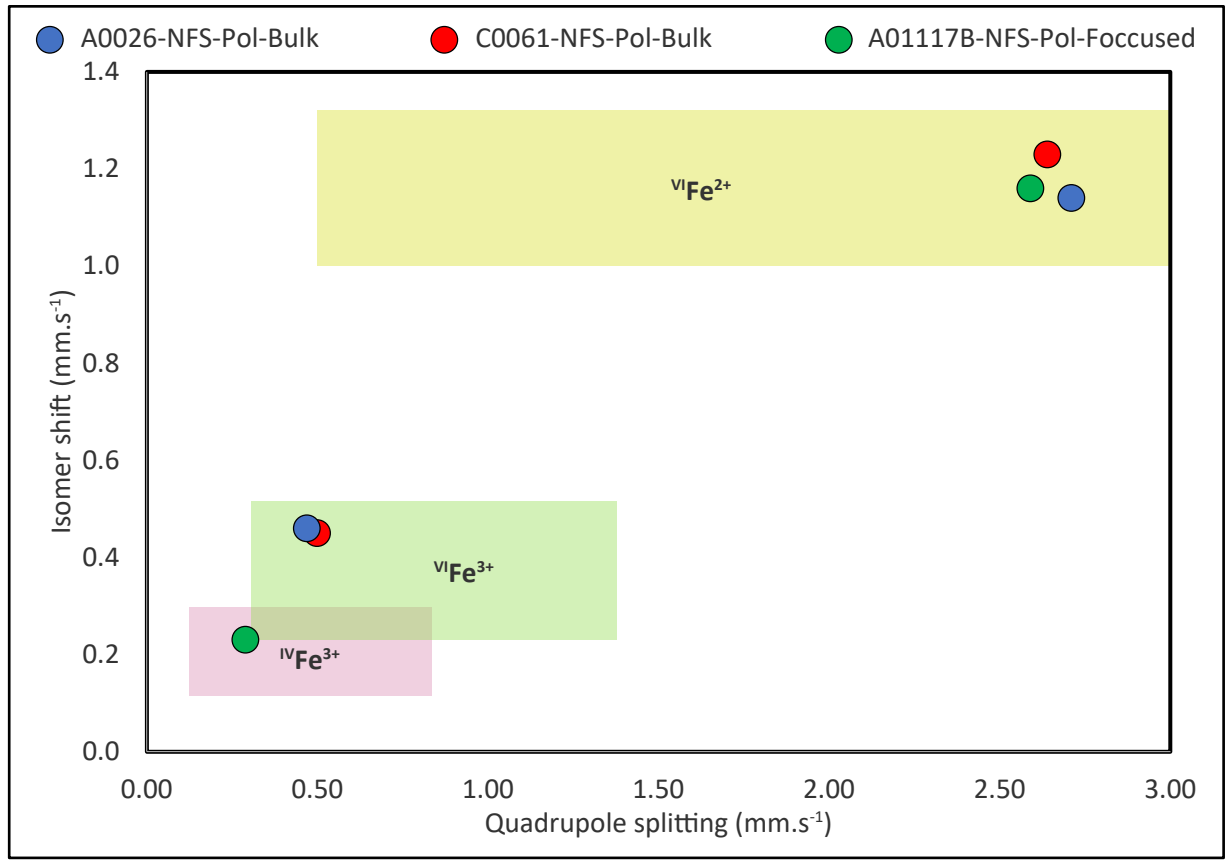
A0026-NFS-Pol-Bulk
C0061-NFS-Pol-Bulk
A01117B-NFS-Pol-Foccused
Isomer shift (mm.s-1)
Quadrupole splitting (mm.s-1)
VIFe2+
VIFe3+
IVFe3+
0.0
0.2
0.4
0.6
0.8
1.0
1.2
1.4
0.00
0.50
1.00
1.50
2.00
2.50
3.00